Master's thesis

NTNU
Norwegian University of Science and Technology
Faculty of Natural Sciences
Department of Materials Science and Engineering

Phillip Michael keck

DFT Study of the Defect Chemistry in the Lithium-Garnet LLZO with Dopants Al, Zn, and Mg

Master's thesis in MT3900 - Structural Chemistry
Supervisor: Sverre Magnus Selbach
June 2020

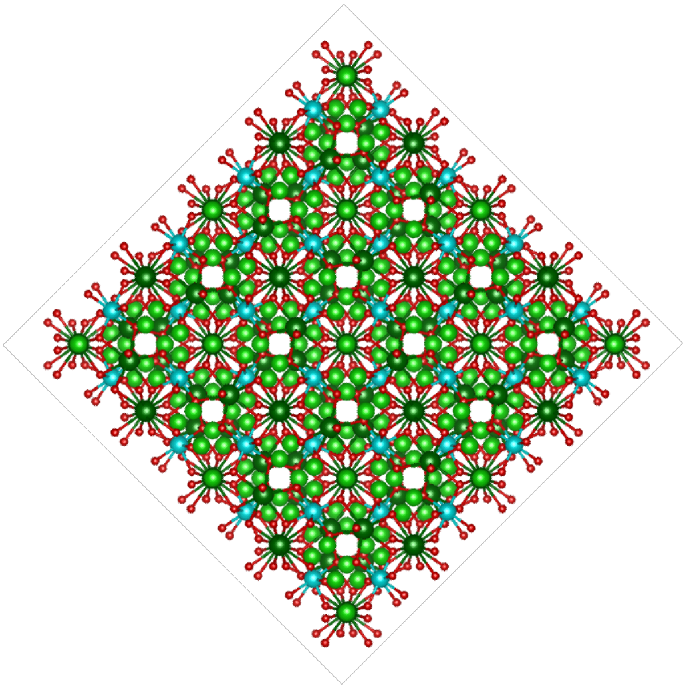

NTNU
Norwegian University of
Science and Technology

Phillip Michael keck

DFT Study of the Defect Chemistry in the Lithium-Garnet LLZO with Dopants Al, Zn, and Mg

Master's thesis in MT3900 - Structural Chemistry
Supervisor: Sverre Magnus Selbach
June 2020

Norwegian University of Science and Technology
Faculty of Natural Sciences
Department of Materials Science and Engineering

NTNU
Norwegian University of
Science and Technology

Abstract

The garnet $Li_7La_3Zr_2O_{12}$ (LLZO) is a leading material in the search for an effective electrolyte material in the solid-state Lithium battery. Aliovalent dopants such as the well-known Al have been shown to stabilize the cubic phase, which boasts high ionic conductivity alongside other desirable properties. Mg and Zn have received little attention as dopants, even though they are cheap, abundant, and boast favorable properties as detailed in previous studies. Using DFT methods, this study aims to show the favorable structural, electronic, and lithium migration properties of the addition of Al, Mg, and Zn metals as dopant species. Systematic substitution at potential cation sites with each dopant is assessed with comparisons to native defects, V_{Li} and Li_i, within the LLZO framework. The distortions and formation energy will be calculated for each dopant to gain insight into favorable dopant properties that will stabilize the desired cubic phase. The nudged elastic band (NEB) method is attempted to calculate the migration barrier energies. Density of States further clarifies the electronic structure and provides insight into the defect state distribution.

A comprehensive study of the site preference and defect chemistry were analyzed for each of the three dopants by substitution at each of the cations. The preferred substitution site for each of the dopants was the tetragonal Li (8a) site according to the calculated formation enthalpy, which was contradictory to initial estimates. The Li vacancy mechanism of charge balance at the octahedral Li (16f) site corresponded to a lower energy than the addition of interstitials at 16e vacancy sites. The lowest energy conformation was Mg doped at the Li (8a) site with 1.34 eV and the Al-doped structure was at 1.35 eV. Formation enthalpy values at the La site implies potential competitive substitution with the Li sites. Zr surpasses the standard energy cutoff of 2 eV to be deemed feasible, which is contradictory to a number of previous studies' findings. After further consideration, it is thought that alternative vacancy formations, such as oxygen or interstitial substitution at low energy sites may have resulted in more optimized calculations. Displacement was directly correlated to the formation enthalpy in most cases, with higher total cell displacement trending towards higher energies. Density of States calculations revealed the absence of defect gap states that would have been detrimental to electrolyte performance. NEB calculations were unsuccessful and deemed inadequate to describe the system.

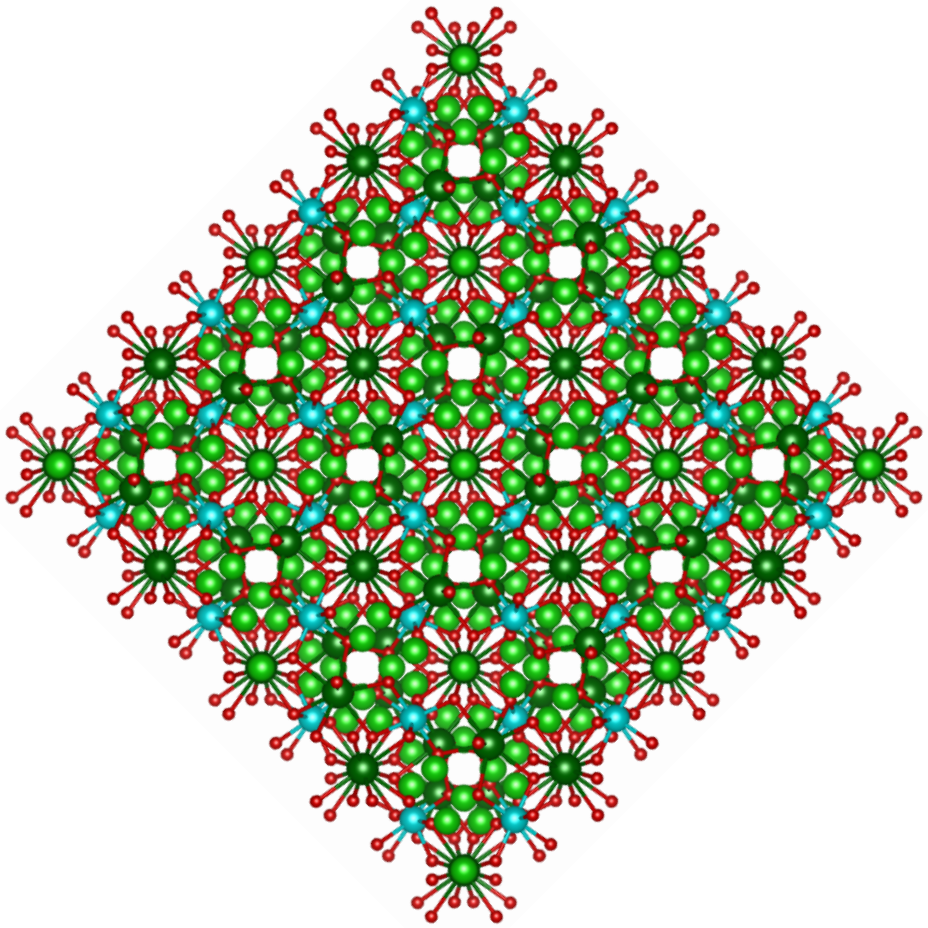

Acknowledgements

A great thanks is given to the many faculty, students, and staff that have made this project possible. My gratitude goes especially towards Fride Vullum-Bruer for encouraging me to apply to NTNU and guiding me in my initial stages of the project. Sverre Magnus Selbach for directing me through the difficulties of adapting to the dark magics of computational science, and Sondre Kvålvag Schnell for aiding in the final delivery of my thesis work. Thanks go as well to Benjamin Williamson and Didrik Småbråten for their extensive help in the many technical and theoretical details I struggled to understand. Lastly, I appreciate the opportunities and resources that NTNU, fakultet Naturvitenskapet, the FACET group, and the IMA department have provided to help me reach the conclusion of this project.

Contents

List of Figures

List of Tables

Symbol List

Symbol	Units	Description
c	mol/g	concentration
D_Li	cm^2S^{-1}	Lithium Diffusion Coefficient
D_0	cm^2S^{-1}	Pre-exponential factor
Δ	n/a	Absolute deviation
∇	n/a	Del operator. Gradient of a vector field
E	kJ	Total Energy
E_A	eV	Activation Energy
E_f	eV	Formation Enthalpy/Defect formation energy
H	n/a	Hamiltonian operator
m	kg	mass
Ψ	n/a	Eigenvalue symbol
ψ_k	n/a	Eigenvalue in reciprocal space
q	n/a	charge
r	Å	radius
σ	S/m	ionic conductivity
S	J/K	Entropy
T	K	temperature
T|n(r)|	J	Kinetic energy of non-interacting electrons
U	J	Potential energy
v	s^{-1}	vibrational freqency
V	Å	Volume
V_H	kJ	Hartree Potential
V_{XC}	kJ	exchange-correlation potential
z_{eff}	n/a	displacement index
μ	eV	chemical potential
Å	10^{-10} m	Angstrom

Constants

$\hbar = 1.054 * 10^{-34}\ m^2\ kg\ s^{-1}$

$\pi = 3.1416....$

$k_B = 1.38 * 10^{-38}\ m^2\ kg\ s^{-2}\ K^{-1}$

1 Introduction

An ever increasing demand for energy in today's modern world has created a concern for sustainable, clean, renewable energy sources. Renewable energy from wind and solar power have grown 244% and 1312%, respectively, in installed energy network capacity[1] between 2010 to 2019. However, both suffer from inconsistent energy production peaks that are reliant on natural weather conditions. This inconsistency in providing a steady source of energy makes them less desirable to energy grid operators than carbon-based fuels. It is therefore essential to develop a means of storing and accessing the large quantity of excess energy harvested during these peak production periods. This serves the dual purpose of supplementing existing energy production capacity by reducing wasted excess energy produced by non-renewables in the course of meeting sometimes unpredictable consumption demands while granting renewables a new level of utility. Rechargeable battery systems also serve in many other capacities that are integrated into the modern world, such as electric vechicles and portable electronics.

Batteries represent a wide range of devices that convert chemical energy to electrical energy through means of voltage-induced ionic transport between two electrodes. The anode is typically the source of positively charged ions that are discharged through a conductive medium known as the electrolyte to the cathode. Here, the excess electrical charge is passed through a current collector to the target destination. Charging can then occur via a voltage-induced current to tranport ions back to the anode. This basic process is shown in the diagram below.

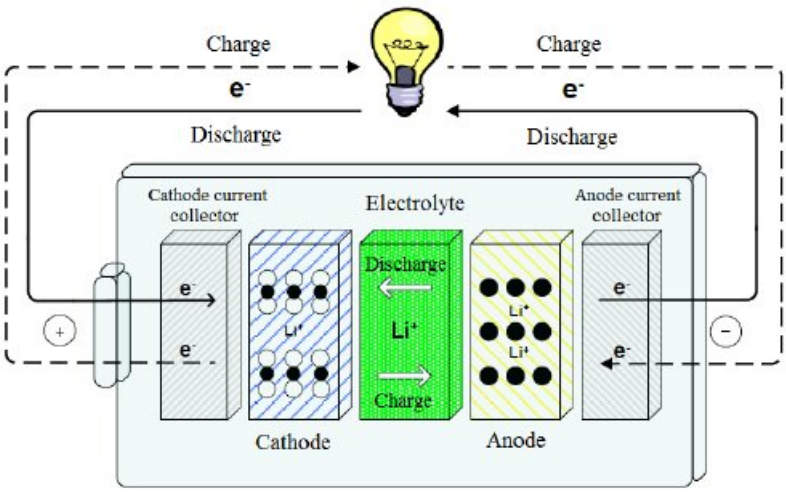

Figure 1: *Diagram of the charge/discharge process in a solid electrolyte Li-battery[2]*

Liquid electrolyte Li-ion batteries were first developed in the late 1970-80's[3]. Since their commercial introduction by Sony in 1991[4], they have become ubiquitous in providing small-scale, portable, electronic storage due to their high energy density relative to other energy storage techniques[5], which earned the developers a Nobel Prize in 2019[3]. However, the current state of the art (SOA) liquid

electrolytes are toxic and volatile organic solvents. Prime quality Li-ion cells are vulnerable to leakage, thermal damage, and short-circuiting due to lithium dendrite formation, all of which lead to severe performance degradation and raise legitimate safety and environmental concerns[5, 6]. These solvents are also reactive with the pure lithium metal anode, which would theoretically allow for the maximum energy capacity a lithium cell could provide. Current SOA anodes utilize a mixture of graphite and lithium, which limits the potential energy density, but prevents the technical issues and high costs associated with a pure lithium anode. Solid state electrolytes circumvent many of the safety and technical issues surrounding Li metal anodes by offering a safer, thermally stable alternative to SOA carbonate-based solvents [7]. However, solid state materials are hindered by sluggish ionic conductivity, one of the primary hurdles to overcome due to the inherently low mobility of ions in solid materials, which leads further to a long series of engineering considerations that need to be managed[5, 6]. Solids come with a laundry list of complex design difficulties of their own as well. The major criteria for a viable solid electrolyte require that it must possess the following properties: high ionic conductivity (10^{-2}-10^{-3} Scm^{-1}, electrically insulating[8], a cost-efficient synthesis method, low interfacial resistance, and relative chemical stability with the anode and cathode materials[9, 10, 11]. Liquid electrolytes have received the bulk of research attention in previous decades due to their high ionic conductivity ($> 10^{-2} Scm^{-1}$), low cost of production, and less complex technical challenges relative to solid electrolytes. Nevertheless, Polymers, ionic liquids, glasses, ceramics, and hybrid composites have all been suggested as potential electrolytes to meet these criteria[6, 8]. Typically, these materials also suffer from poor chemical and electrochemical stability, which hinders their use in practical applications[8]. However, crystalline ceramic oxides are generally easier to prepare and offer excellent thermal stability and mechanical properties compared to other solid electrolytes[5].

The garnet $Li_7La_3Zr_2O_{12}$ (LLZO) has emerged as a leading material in solid state research. It has a complex, garnet-type, crystalline structure that was first reported in 2007[12]. Formation of pure LLZO at high temperature sintering promotes the cubic ($Ia\bar{3}d$ space group no.230) phase, which then crystallizes to the tetragonal ($l4_1/$acd space group no.142) phase through tetragonal distortion during the cooling process[13, 5, 14, 15]. This transition mostly affects the lithium site distribution as opposed to other significant structural changes[13, 15]. The tetragonal phase possesses poor ionic conductivity of 10^-6 Scm^-1, nearly 2-3 orders of magnitude lower than the cubic phase, which is considered one of the prime electrolytes for use in solid-state Li batteries with an ionic conductivity between 10^-3 and 10^-4 Scm^-1[5] depending on the synthesis method and dopant composition[6]. The cubic phase has also been reported to have a wide voltage stability window (>5V vs Li/Li^+) and good chemical stability.[6] Thus, it is desirable to stabilize the cubic phase at low temperatures for use as solid state electrolyte. Fortunately, it was found that even trace amounts of aliovalent dopants can stabilize the cubic phase[5]. After several groups reported concentrations of Aluminum doping at the Li^+ site both unintentionally and intentionally by means of the Al_2O_3 crucible[16,

8], Rangasamy et. al.[17] confirmed that a minimum concentration of 0.204 moles of Al per formula unit was required to stabilize the cubic phase. Thompson et. al.[18] further asserted that this amounted to a critical Li vacancy concentration of 0.4-0.5 Li vacancies per formula unit with site preference for substitution at the Li sites. The Al dopant can be substituted for other aliovalent dopants with differing site preferences, such as M^{5+} (M=Ta,Nb) for Zr^{4+}. However, LLZO forms a passivation layer consisting mostly of LiOH and Li_2CO_3[19, 20], when in contact with air. This layer, known as the surface electrode interface (SEI) increases the resistance and degrades the electrolyte material over time. This is further exacerbated by the formation of lithium dendritic structures at lithium propagation sites through interconnected voids at the grain boundaries[19]. Much effort has been put into suppressing this growth in order to extend the lifetime and aid sintering properties of the electrolyte material[19, 21, 22].

Mg and Zn have received little attention as dopants in the LLZO system, even though they are cheap, abundant, possess favorable ionic properties (i.e. radius, electronegativity), and have been shown to have good thermodynamic stability and site preference compared to other potential dopants in the LLZO system[23]. Using Density Functional Theory (DFT), this study aims to show the favorable structural, electronic, and lithium migration properties of Al, Mg, and Zn relative to one another in the LLZO crystalline lattice. Systematic substitution at potential cation sites with each dopant is assessed with comparisons to some native defects, V_{Li} and Li_i, within the LLZO framework. The nudged elastic band (NEB) method is used to calculate the migration barrier energies. Density of States (DOS) further clarifies the electronic structure and provides insight into the defect state distribution within the LLZO electronic structure.

2 Materials Considerations

2.1 LLZO Structure

As described in Jain et. al., the symmetrized crystal structures of tetragonal and cubic LLZO both contain 192 ions in their unit cells with the chemical formula $Li_{56}La_{24}Zr_{16}O_{96}$.[24] The tetragonal structure has a Hermann Mauguin point group I41/acd [no. 142] which has four distinct Li Wyckoff sites: one fully occupied tetrahedral Li2 (8a), one fully unoccupied tetrahedral Li(16e) two fully occupied octahedral Li1 (16f) and Li0 (32g). There are also two dodecahedral LaO_8 polyhedra La4 (8b) and La3 (16d) and the ZrO_6 octahedra Zr5 (16c). These are referred to herein by their site labels as Li2, Li1, Li0, La3, La4, and Zr5, respectively.[13, 25] The tetragonal group has full occupancy at all 56 available Li sites (8a, 16f, and 32g) as a result of its high degree of order in the Li sub-lattice. The unoccupied 16e sites are energetically unfavorable as they lie in the conduction band, requiring significant lattice distortion in order to accommodate a temporary lithium occupancy, such as during concerted lithium migration[26]. The cubic $Ia\bar{3}d$ point group [230] has 120 available Lithium vacancy sites over 24 tetrahedral Li0 (24d) sites with an occupancy of 0.96 and partial occupancy by a stabilizing dopant species (in this case, Al). There are an additional 96 octahedral Li1 (96h) sites with an occupancy of 0.34, resulting in disorder and vacancies conducive to a single ion hopping Li migration mechanism[13, 25]. The Li0 (24d) sites are the redistributed 8a and 16e sites from the tetragonal structure while Li1 (96h) sites are the 16f and 32g sites. The La3 and La4 have redistributed to the equivalent cubic La2 (24d) site. Zr3 remains at the 16c site.

Tetragonal	**Wyckoff**	**CN**	**Occ**	**Cubic**	**Wyckoff**	**CN**	**Occ**
Li2	8a	IV	1	**Li0**	24d	IV	0.96
Li	16e	IV	0	**Al**	24d	IV	0.04
Li1	16f	VI	1	**Li1**	96h	VI	0.34
Li0	32g	VI	1	–	–	–	–
La4	8b	VIII	1	**La2**	24d	VIII	1
La3	16d	VIII	1	–	–	–	–
Zr5	16c	VI	1	**Zr3**	16c	VI	1

Figure 2 displays both the tetragonal and cubic cell side by side. Li atoms bridge the corner and La atoms the edges in the tetragonal cell, while Zr evenly occupies the edges, corners, and faces of the cubic structure. The partial occupancies of Li1, Li0 and Al-sites are visualized as partial white/green/blue spheres to represent the disordered distribution across sites. The position of the overlapping orbitals is determined by the positions of the Li-Li pairing. It is this disorder and random structuring throughout the lithium sub-lattice that grants LLZO its enhanced ionic conductivity. More lithium migration pathways are freely available in three-dimensional space. The tetragonal is limited in its 3D Li mobility by 16f sites that block the free migration of Li except at high temperatures[15]. The full

discussion on the cubic phase transition can be found in chapter6.5. The polyhedrals for the tetragonal and cubic phases can be found below in Figure 3 and Figure 4, respectively.

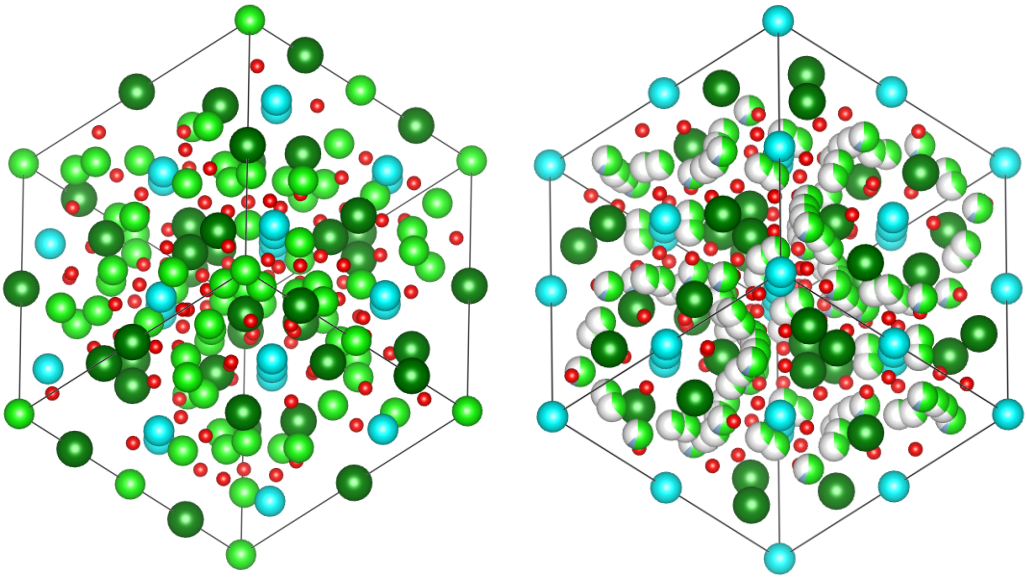

Figure 2: *(left) Conventional 196 atom LLZO unit cell[24]. Bright green atoms represent Li, Dark green is La, and light blue is Zr. (right) 196 atom Al-doped cubic LLZO unit cell[27]. Gradient white and green orbs represent partial occupancy orbitals of Li1- and Al-sites.*

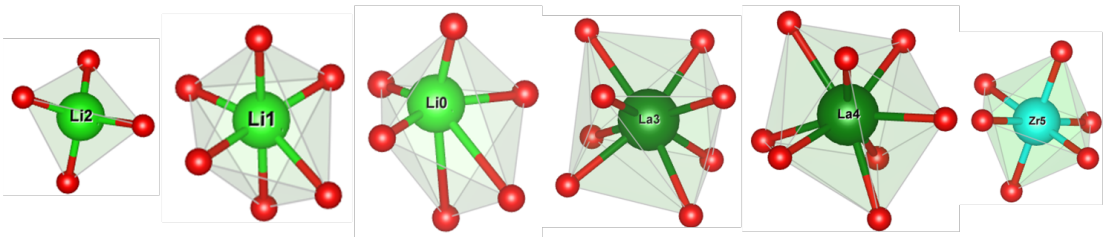

Figure 3: *(Left to right): Li2, Li1, Li0, La3, La4, and Zr5 Polyhedra in the Tetragonal LLZO structure*

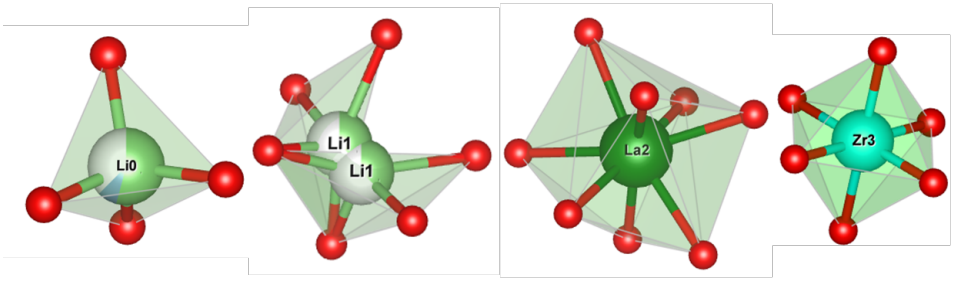

Figure 4: *(Left to right): Li0, Li1, La2, and Zr3 Polyhedra in the cubic LLZO structure*

2.2 Defects and Lithium Migration

Lithium migration through the garnet-type lattice is quite complex and the pathways are not fully understood. Due to the highly ordered Li ion lattice in Tetragonal LLZO, migration of Li ions most likely occurs by a fully collective or synchronous motion known as concerted migration. This mechanism involves the reconfiguration of atoms neighboring correlated migrating Li atoms to accommodate their mobility, which inherently has a high activation energy cost since there is induced simultaneous motion in atoms throughout the lattice.[25, 26, 28, 29]. Concerted migration occurs as a result of restriction on the occupied site-to site interatomic separation and the unstable residency of Li atoms at the 8a site between the unoccupied 16e site[25, 26, 28, 29]. The primary mechanism for lithium in cubic LLZO is single-ion hopping due to weak site dependence of the lithium atom, resulting in a higher ionic conductivity and lower activation energy costs[25, 28, 29].

In Vegard's law, a linear relation exists at constant temperature between the crystal lattice constant of a given alloy and the concentrations of the contstituent elements[30, 31]. This has been shown to hold true given that the atomic size of the mixing alloy is of an approximate size to the constituent crystal lattice particles in a simple, binary mixture of hard spheres. Previous studies[32, 13] have assumed this as an adequate method for experimental structural calculations regarding the crystal lattice alloy mixing within the LLZO crystal lattice. The direct-charge-compensation model used in the current study assumes a direct formation of Lithium vacancies or interstitials to account for the charge imbalance resulting from aliovalent substition. In the following example, this is denoted by the Kröger-Vink notation for aliovalent substitution of Al at the Li site, although this same model can be applied to dopants with varying oxidation states at any of the sites within the lattice structure:[33]

$Al_{Li}^{\bullet\bullet} = {}_2V_{Li}'$

This method models ideal synthesis conditions, and is not completely accurate to realistic defect formation. Recent studies have expanded on the model by iterating over a series of potential Fermi energies that simulates different synthesis conditions, such as an oxygen or Li rich environment, to show the dependency of defect formation energy on the self-consistent Fermi level[34, 35]. V_{Li} and Li_i

typically dominate defect formation in tetragonal LLZO. Oxygen vacancies have sometimes been shown in previous literature to be directly involved in balancing the Li content, even increasing the total Li content as Li_{Zr} antisites dominate the stoichiometry[34]. However, for the scope of the current study, a basic description of a single defect environment is sufficient to compare the formation energies, lattice distortion, and lithium migration energy barriers.

2.3 Dopants

Aluminum is the most common and extensively researched dopant species for LLZO, but this is largely incidental, due to its abundant presence in the calcination and sintering process. It is crucial to examine a wide range of dopants, as different cations and even some anionic[36] species may optimize LLZO's compatibility for certain implementations or use with different cathode materials[23]. Since the stabilization of the cubic phase appears to be most directly linked with Li disorder, which is unlikely to occur solely from steric effects, it most likely stems from a change in lithium content [15, 26, 23, 37] or other vacancies[34, 35] that do not favor isovalent substitution[23].

Miara et. al.[23] presented an exhaustive study detailing defect energy and site preference of all possible dopants in the LLZO system. Mg and Zn, both of which have to date only been lightly explored[37, 38, 39], were novel dopants at the time of the publication, showing high site preference and low defect energy at the Zr- and Li-sites, respectively. This challenges more established dopants such as Al^{3+}, Ga^{3+}[40], Fe^{3+}[41], Nb^{5+}[42], Ta^{5+}[40], and Y^{3+}[43]. They further equate a low defect formation enthalpy with high lattice solubility, implying a lower crystal lattice distortion and thus a high dopant concentration. The high Al content at Li dopant sites may actually hinder Li-ion mobility in the Li sub-lattice and create higher grain boundary resistance, while higher valence dopants in high quantity induce excessive V_{Li} that deprive the electrolyte of Li content vital to fast ionic transport[40]. The ionic radii of Mg and Zn are comparable to Li[44], implying a minimum steric effect that still introduces vacancies into the system. Aluminum has a smaller ionic radius as well as a higher charge, which may account for the higher steric displacement observed in the current study.

The Mg-doped structure has further been reported to reduce the sintering temperature from 1200°C to 1000 °C and halving the time required[38]. The reported sintering characteristics also reduced the grain size and internal resisistance along grain boundary lines[38]. These characteristics greatly reduce associated cost and increase viability in commercial production. A cursory study also reported increased composition-phase stability upon exposure to atmosphere and moisture[39]. Formation of the passivation layer from decomposition of the electrolyte, particularly at the cathode/anode surface, is known as the solid electrolyte interface (SEI). This film prevents further reaction with the electrode materials, stabilizing the interface, but increases interlayer resistance and suppresses Li-ion conductivity[39]. An abundantly thick SEI layer can further promote lithium dendrite formation in the electrolyte material by increasing the energy barrier to cross

Table 1: *Ionic Characteristics for each atomic species*

Species	Charge	CN	Ionic Radius Å	Electronegativity
Li	+1	IV	0.59	0.98
		VI	0.76	
La	+3	VIII	1.16	1.10
Zr	+4	VI	0.72	1.33
O	-2	VI	1.4	3.44
Al	+3	IV	0.39	1.61
		VI	0.54	
Mg	+2	IV	0.57	1.31
		VI	0.72	
Zn	+2	IV	0.6	1.65
		VI	0.74	

between the electrolyte and electrode materials. Lithium dendrites are jagged accumulations of Li atoms that form along grain boundaries, degrading cell quality and sometimes leading to short-circuits, effectively mitigating a major advantage of the solid electrolyte. One previous study compared Zn and Al computationally due to their difference in family, group, content, and valences[37]. Their conclusions are unraveled in the following paragraph. Zn is expected to demonstrate exceptional capabilites when substituted at the Li-site with a reported defect energy of 1.32 eV, lower than Al[23, 37].

Substitution at the Li2 (8a) site is reported to highly suppress the Li pathway as it "traps" nearby active octahedral sites by blocking available Li migration pathways, effectively decreasing the chance that nearby octahedral sites will participate in Li migration. Theoretically, this requires higher activation energies to overcome the electrostatic repulsion present at the four nearest influenced sites, making them unfavorable for Li-ion occupation[37, 45]. Furthermore, they suggest that the lack of vacancies created by Zn substitution severely limits nearby lithium migration pathways in the cubic phase, but this is only when using the same doping levels. This seems to be a major flaw, since the divalent Zn would obviously need more material precursor to achieve the same vacancy concentration as the trivalent Al, when taking charge balance into account. Actual defect formation energies place the substitution of several dopants at the Li2 site >100meV less than the Li1 or Li0. Their study also neglected to examine further site distributions, such as alternative Li, La, and Zr sites. Furthermore, they ignore the redistribution of Li site occupancy that occurs as a result of the phase change[15]. While doping at the Li2 site may block pathways in the tetragonal lattice, the weak site dependency of the cubic phase ensures that the dopant and Li atoms have a limited amount of freedom to reconfigure, ensuring maximum mobility of the 3D Li migration pathway[15].

Zn and Mg are abundantly available in the Earth's crust and cheaply obtained in comparison with more expensive rare earth metals, such as Nb, Y, Ta, etc[46]. They most likely possess similar or better characteristics. As such, these dopants

warrant further study. Below is the proposed set of direct-charge-compensation mass balances:

$$\mathrm{Mg}^{\bullet\bullet} \longrightarrow \mathrm{Mg}_{\mathrm{Li}}^{\bullet} + \mathrm{V}'_{\mathrm{Li}} \qquad \mathrm{Al}^{\bullet\bullet\bullet} \longrightarrow \mathrm{Al}_{\mathrm{Li}}^{\bullet\bullet} + 2\,\mathrm{V}'_{\mathrm{Li}}$$

$$\mathrm{Zn}^{\bullet\bullet} \longrightarrow \mathrm{Zn}_{\mathrm{Li}}^{\bullet} + \mathrm{V}'_{\mathrm{Li}} \qquad \mathrm{Mg}^{\bullet\bullet} \longrightarrow \mathrm{Mg}''_{\mathrm{Zr}} + 2\,\mathrm{Li}_{\mathrm{i}}^{+}$$

$$\mathrm{Zn}^{\bullet\bullet} \longrightarrow \mathrm{Zn}''_{\mathrm{Zr}} + 2\,\mathrm{Li}_{\mathrm{i}}^{+} \qquad \mathrm{Al}^{\bullet\bullet\bullet} \longrightarrow \mathrm{Al}'_{\mathrm{Zr}} + \mathrm{Li}_{\mathrm{i}}^{\bullet}$$

$$\mathrm{Mg}^{\bullet\bullet} \longrightarrow \mathrm{Mg}'_{\mathrm{La}} + \mathrm{Li}_{\mathrm{i}}^{\bullet} \qquad \mathrm{Zn}^{\bullet\bullet} \longrightarrow \mathrm{Zn}'_{\mathrm{La}} + \mathrm{Li}_{\mathrm{i}}^{\bullet}$$

$$\mathrm{Al}^{\bullet\bullet\bullet} \longrightarrow \mathrm{Al}_{\mathrm{La}}$$

The addition of interstitials alone is unlikely in the physical sense due to a prohibitive defect energy. A more likely model would involve a $\mathrm{V}_{\mathrm{O}}^{\times}$ accompanied by a $\mathrm{V}_{\mathrm{Li}}^{\times}$ to achieve the charge balance. This creates the necessary lithium disordering with a lower activation energy while retaining a high lithium content.

3 Density Functional Theory

Density Functional Theory (DFT) is an *Ab initio* method to model the thermodynamic properties of materials using quantum mechanical laws and theorems. This allows for isolated observations of the electronic structure of matter at the nanoscale without the need for prior empirical data. This chapter is intended to give a brief overview of the concepts discussed and explored within the current project. In particular, the utility and theory behind Nudged Elastic Band (NEB) and Density of States (DOS) methods will be introduced due to the wealth of information they provide for electrolyte materials in battery applications. For further clarification of the theories presented, please refer to the more detailed works[47][48] that have succinctly summarized the complex quantum mechanical theories and their derivations. The *Vienna Ab Initio Simulation Package* (VASP)[49, 50, 51, 52] was used to carry out the calculations in this project, and as such, a brief explanation is included at the end of the chapter. The full list of variables referenced here and in the following chapters can be found on page viii of the preface.

3.1 The Schrödinger Equation

To describe a well-defined collection of atoms forming a particular crystal structure, it is necessary to calculate their energy and the change in energy when these atoms change position. Since the nuclei, which is composed of protons and neutrons, is orders of magnitude heavier than individual electrons, their motion can be assumed independent of one another. Solving for the nuclei as fixed positions that create an external electrostatic field as a result of their Coulombic potential and finding the ground state energy of a set of electrons moving in this field, one can separate these into two distinct mathematical problems. This is known as the Born-Oppenheimer approximation[53]. This relation is represented by the eigenvalue $\Psi(r_1, r_2, ..., r_i)$. In which r_i is the position and spin of a given particle i.

The Schrödinger equation forms the basis for understanding the electronic structure of matter for a multi-electron wave function. The time-dependent form relates the temporal and spatial derivatives of $\Psi(x,t)$ with the potential energy function V(x,t)[54]:

$$\frac{\hbar^2}{2m}\frac{\partial^2\Psi(x,t)}{\partial x^2} + V(x,t)\Psi(x,t) = i\hbar\frac{\partial\Psi(x,t)}{\partial t} \tag{3.1}$$

Using the Born-Oppenheimer approximation, this is simplified to the time-independent Schrödinger equation that can be broken down into its constituent terms as below, from left to right: the kinetic energy operator, the potential energy operator between each electron and the electrostatic potential from the nuclei, and the potential energy operator due to repulsive electron-electron interaction[47].

$$\left[\frac{\hbar^2}{2m}\sum_{i=1}^{N}\nabla_i^2 + \sum_{i=1}^{N}V(r_j) + \sum_{i=1}^{N}\sum_{j<i}U(r_i,r_j)\right]\Psi = E\Psi \tag{3.2}$$

Ψ is the total electron wavefunction, E is the ground state, V is the volume, U is the Potential energy, ∇ is known as the "del operator", and m is the electron mass. The total wavefunction can be approximated as a product of the individual electron wavefunctions $\Psi = \Psi_1(r)\Psi_2(r), ..., \Psi_N(r)$, and is known as the Hartree product. However, the system quickly becomes too complex as there are many electrons per atom and 3 dimensions per electron. A wavefunction for a particular point in space cannot be directly observed, but instead it is measured by the probability that a set of N electrons is present in a given location $\Psi^*(r_1, ..., r_N)\Psi(r_1, ..., r_N)$. Similarly, the density of electrons n(r) at a given position is

$$n(r) = 2\sum_i \Psi_i^*(r)\Psi_i(r) \tag{3.3}$$

Given the computational strain that these calculations would ensue, in practical terms it is necessary to create accurate, analytical descriptions of a system using approximations.

3.2 Hohenberg-Kohn Theorems

Density functional theory is derived from two mathematical theorems proved in 1964 by Kohn and Hohenberg.[55] The first theorem states that *The ground-state energy from Shrödinger's equation is a unique functional of the electron density.*[47]

$$E_v[n] \equiv \int v(r)n^{'}(r)dr + F[n] \tag{3.4}$$

F[n] is a universal function, valid for any number of particles and any external potential, and v(r) is the given potential. At a certain value of n(r), $E_v[n] = E_0$. This functional puts the Schrödinger equation in terms of the three spatial coordinates of electron density as opposed to the 3N variables of the wave function. The second theorom helps to elaborate on the form of the energy functional: *The electron density that minimizes the energy of the overall functional is the true electron density corresponding to the full solution of the Schrödinger equation* This variational principle still leaves the exact functional F[n] undefined or without a proper approximation.

3.3 The Self-Consistent Kohn-Sham Equations

The Kohn-Sham approach[56] handles the exchange funtional, F[n], by separating it into three separate functionals that can be solved by single-electron wave functions that depend only on the spatial variables, $\Psi_i(r)$ and do not interact with one another. When applied to the summations in equation 3.2, it appears as

$$\left[\frac{\hbar^2}{2m}\nabla^2 + T[n(r)] + V_H[n(r)] + V_{XC}[n(r)]\right]\Psi_i(r) = \epsilon_i\Psi_i(r) \tag{3.5}$$

where T[n(r)] is the kinetic energy of a system of non-interacting electrons, V_H is the Hartree potential, and V_{XC} is the exchange-correlation energy of an interacting

system, each of these a density n(r). The first is the 'known' energy of the system that is composed of electron kinetic energies and coulombic interactions between electron-nuclei, electron-electron, and nuclei-nuclei. The Hartree potential is the total interaction between all electrons within the system and is expressed in the following equation:

$$V_H(r) = e^2 \int \frac{n(r')}{|r - r'|} d^3r' \tag{3.6}$$

This includes self-interaction that is corrected in the exchange correlation potential term:

$$V_{XC}(r) = \frac{\partial E_{XC}(r)}{\partial n(r)} \tag{3.7}$$

There are still several unknowns with this method, starting with V_XC, and the solution is a circular process. This can be overcome by an initial guess for n(r) and then subsequent iterations until convergence within set parameters occurs at the density necessary to achieve minimization of the ground-state energy.

3.4 The Exchange-Correlation Functional

In order to solve the Kohn-Sham, the exchange-correlation functional needs to be known, but to date it is still unknown. The simplest approximation of the functional uses the known $V_{XC}^{electrongas}$ where the electron density is uniform throughout an electron gas and the local density n(r) to give an approximation. This is the local density approximation (LDA). Other functionals have been developed to better describe specific physical systems, such as GGA, which includes a local gradient in the electron density. While this includes more physical information, the implementation of the gradient needs to be specifically adapted to describe certain physical solutions. PBEsol[57] is a GGA functional that shows adequate approximation in a solid and is the functional method that has been used in the current study.

3.5 Hellmann-Feynman Forces

Once this minimized state is found through this iterative process, the forces on the ions are calculated, allowing for the movement of ions based on these calculated forces. These Hellman-Feynman[58, 59] forces take into account the the partial derivative of the energy calculated by the Kohn-Sham equations with respect to any parameter λ. The relation is described by the equation

$$\frac{\partial E}{\partial \lambda} = \langle \Psi^* | \frac{\partial V}{\partial \lambda} | \Psi \rangle \tag{3.8}$$

This is used to determine the minimized crystal structure in the current system after doping, by reducing the overall forces acting on each ion to their lowest extent. When the ions adopt a new configuration, the convergence is repeated until they reach an equilibrium state.

3.6 Practical DFT Approaches

Given the complexity of calculations within a single system, there is no doubt that conserving computational resources is vital to reducing expense of a process. Many parameters and algorithms have been designed to optimize the process and ensure only required information is generated.

3.6.1 K-points and the Brillouin Zone

Given the cost of intensive computational studies, a full bulk material must be limited to a finite number of atoms that still describe the overall system to a degree of accuracy and precision. The supercell defines the most basic input to a DFT calculation and defines the shape and volume of the arrangement of atoms in periodic space[47]. This is defined by the lattice vectors, which describe the length of the sides of a rectangular periodic box in the x, y, and z direction, denoted by a, b, and c. The primitive unit cell is the smallest number of atoms that compose an identical symmetrical section of the bulk lattice capable of fully defining the periodic material infinitely in every direction. Thus, the primitive unit cell is the supercell that is sufficiently large enough to describe the internal interactions of the lattice.

The solution to the Schrödinger equation for this periodic system must satisfy Bloch's theorem:

$$\phi_k(\boldsymbol{r}) = exp(i\boldsymbol{k} * \boldsymbol{r})u_k(\boldsymbol{r}) \tag{3.9}$$

where $u_k(r)$ has the same periodicity as the supercell. This allows for the solution to value of $\boldsymbol{k}$ independently. $\boldsymbol{k}$ represents reciprocal space and $\boldsymbol{r}$ represents real space. K space is more convenient to tackle the mathematical problems in DFT, so using the Wagner-Seitz primitive cell with reciprocal lattice vectors creates the Brillouin zone, which has many properties that are central to the band theory of materials[47]. In particular, this eases the calculation of evaluating integrals defined in reciprocal space that integrate only over possible values of $\boldsymbol{k}$ in the Brillouin Zone, reducing cost for larger cells by iterating over a finite number of k-points. An in-depth definition of the integrals and further k-point theory can be found in chapter 3.1 of reference[47]. The primitive cell in real space is related by

$$V_{BZ} = \frac{(2\pi)^3}{V_{cell}} \tag{3.10}$$

where V_{BZ} is the volume of the Brillouin Zone

3.6.2 Energy Cutoff

$u_k(r)$ can be expanded relative to a set of plane waves:

$$u_k(\boldsymbol{r}) = \sum_G c_G exp[i\boldsymbol{G} * \boldsymbol{r}] \tag{3.11}$$

which summates over all vectors defined by $G = m_1b_1 + m_2b_2 + m_3b_3...m_ib_i$. Combining the equation above with equation 3.9 yields

$$\phi_k(r) = \sum_G c_{k+G} exp[i(\boldsymbol{k} + \boldsymbol{G})\boldsymbol{r}] \tag{3.12}$$

To avoid an infinite number of summations, solutions with kinetic energy can be applied

$$E = \frac{h^2}{2m}|\boldsymbol{k} + \boldsymbol{G}|^2 \tag{3.13}$$

Applying the energy cutoff parameter:

$$E_{cut} = \frac{h^2}{2m}G_{cut}^2 \tag{3.14}$$

Convergence testing as described in section 4.2 is necessary to find the lowest possible value for the energy cutoff without obtaining divergent total energies in the results.

3.7 Electronic Density of States

The electronic density of states (DOS) describes the electronic states of a material by the concentration of occupied or unoccupied states in the form of atomic orbitals.[47] The DOS is determined by integrating the electron density, from a static DFT calculation, in k space. It is important in systems with fewer atoms to have a high k-point density to accurately sample the reciprocal space. In the context of LLZO, this is not necessary as it already has a dense band structure composed of many atoms, so increasing the k-mesh only practically increases convergence time.

The electronic states occupy two regions in the DOS diagram, the valence and the conduction bands. The valence band is the collection of all occupied states and the conduction band is filled with all the unoccupied states at 0K. The energy in DOS diagrams is mapped relative to the highest occupied electronic state, known as the Fermi energy. In electronically insulating materials, such as the electrolyte LLZO presented in this study, there are ideally no available states for excited electrons above the Fermi energy, so the DOS at the Fermi energy is usually directly at zero. Between the two band regions, there is typically an energy range devoid of any electronic states, known as the band gap. This is the amount of energy in eV that it would take to excite an electron into the lowest unoccupied orbitals in the conduction band. For an electrolyte material, this number would ideally be as large as possible to prevent short circuiting and electronic conductivity. Minimizing the electronic conductivity is a primary goal in developing electrolyte materials as this builds up high resistance in the cell that creates undue heating and blocks ion transport. Another sign of an insulating material are the separated energy bands with energy gaps between them. Below in Figure 5, a comparison can be made between metallic, semiconducting, and insulating materials. Since it is only necessary to discuss the nature of insulating materials in relation to LLZO,

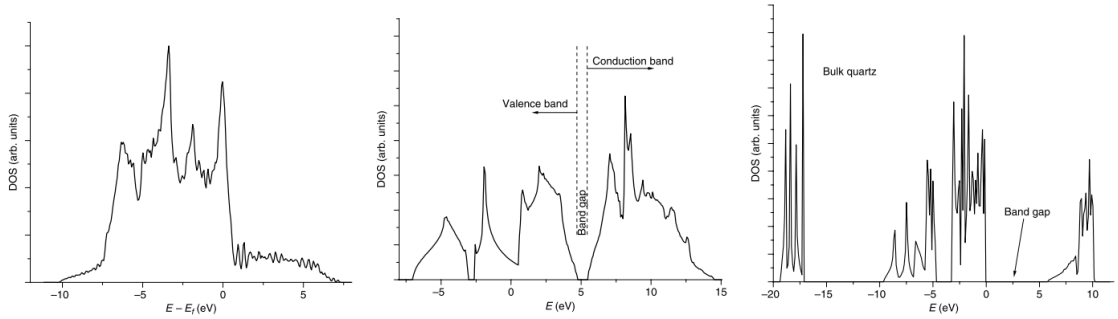

Figure 5: *(Left) Metallic Pt DOS (Mid) DOS for semiconducting bulk Si showing the valence and conduction bands as well as the band gap. (Right) DOS for insulating bulk quartz material*

a full discussion of the metal and semiconducting DOS can be found in chapter 8 of ref. [47].

Of particular importance to defect chemistry is the distribution of occupied orbitals of the dopant and perturbed atoms in the structure. It is necessary to define the electronic structure in order to determine what effects the dopant species may have on on both occupied and unoccupied electronic states following relaxation.

3.8 Transition State Theory

Transition state theory (TST) is fundamental to understanding the migration energy barriers of Lithium ions in the LLZO lattice[47]. used to calculate the rate of diffusion, but this These can be calculated by allowing an ion to move through the bulk material into lithium occupancy sites while allowing all the atoms in the material to relax. A path between the two energy minimum sites is composed of a number of interpolated images, typically five to seven, that effectively model the lithium ion in intermediate positions. More images will yield more accurate results but greatly increase computation costs. The resulting calculated energy along the minimum energy path represents the activation energy barrier for the migration process. These images act as an initial guess at the final energies, but a simply interpolated image set may be far from the actual energies. Thus, techniques such as the image dependent pair potential (IDPP)[60], which uses bond distances between the atoms involved as opposed to linear interpolation of positions, can be useful to more accurately guess the initial energies. In most cases, this greatly decreases the number of iterations to reach convergence. Another important method that will come into play is the climbing image method[61], which fixes the highest energy image to the energy maximum. This image does not feel spring forces as a result. This method primarily serves to acquire more evenly distributed data sets.

The other main purpose of TST is to calculate the rate of diffusion. This can be done by finding the energy of the saddle point between two energy minima and the vibrational frequency (v) of the ion in the potential minimum, which also be roughly estimated by using the typical atomic vibration v $= 10^12 - 10^13s^{-1}$. The

simplified form of the equation for the rate, the harmonic transition state theory:

$$k_{A-->B} = v\ exp(\frac{E^{\dagger}\ E_A}{k_B T}) \tag{3.15}$$

This allows a rough of general ionic conductivity for each structure, which will be valuable in comparing the different dopants. Further expanding this expression to a multidimensional transition state in which the ion can sample nearby sites outside the targeted path, the following equation is obtained

$$k_{A-->B} = \frac{v_1 * v_2 ... * v_N}{v_1^{\dagger} * ... * v_N^{\dagger}} exp(\frac{\Delta E}{k_B T}) \tag{3.16}$$

Where $v_N^{\dagger}$ is the real vibrational frequency associated with the transition state as opposed to the energy minimum.

3.8.1 Elastic Band method

The elastic band method is based off early "chain-of-states" theories, in which the minimum energy path (MEP) between two local minima is defined. Elastic attempts to use lowest amount of energy and evenly spaced images, which can be explained by the nonlinear function

$$M(\vec{r}_P) = \sum_{i=1}^{P-1} E(\vec{r}_i) + \sum_{i=1}^{P} \frac{K}{2}(\vec{r}_i - \vec{r}_{i-1})^2 \tag{3.17}$$

where r_P represents the set of images, P is the number of images, K is the stiffness of the harmonic springs that connect adjacent images, and $E(r_i)$ is the total energy of ith image. This has two major issues. The first is stretching, whereby the images do not exhibit high enough energy as a result of an incorrect stiffness for the elastic bands. In the second problem, corner cutting, images take a longer route, thus not passing through the true MEP and arriving at an overestimation of the activation energy.

3.8.2 Nudged Elastic Band

The nudged elastic band method improves upon these issues by computing the force acting on the system $\hat{F}_i = \nabla E(\hat{r}_i)$ and ensuring that the images are only acted upon by the perpendicular components of these forces. The direction of the path betweeen two images can be expressed as a unit vector $\hat{\tau}_i = \hat{r}_{i+1} - \hat{r}_{i-1}$. The perpendicular forces acting on the images can then be expressed by $\hat{F}_i^{\perp} = \hat{F}_i - (\hat{F}_i * \hat{\tau}_i)\tau_i = 0$. By applying negative spring forces parallel to the band, the forces only act to keep the images evenly spread along the path and prevent them from pulling away from the MEP. This is defined by the following equation:

$$\hat{F}_{i,spring}^{\parallel} = (\hat{F}_{i,spring} * \hat{\tau}_i)\hat{\tau}_i \tag{3.18}$$

which can then be added to the perpendicular froces to arrive at updated positions

$$\hat{F}_{i,update} = \hat{F}_i^{\perp} + \hat{F}_{i,spring}^{\parallel} \tag{3.19}$$

The calculation has converged when the updated forces are zero, corresponding to all images lying along the MEP. The transition state energy should lie at the saddle point of the resulting energy curve.

3.9 Limitations of the DFT Method

A feasible DFT calculation does not fully solve for the Schrödinger equation, as the functional described in the Hohenberg-Kohn theorem is not yet known. As such, there is a certain amount of uncertainty between DFT and true ground-state energies. However, DFT solutions are close enough to provide reliable insight into scientific questions and can be compared against experimental values to determine the degree of uncertainty in the results.

It is important to understand under which situations DFT performs poorly. DFT calculations of excited electronic states generally results in limited accuracy. The theorems only apply to the ground-state, meaning that predictions made for higher energy levels will inherently be more prone to uncertainty.

The second problem lies with the underestimation of calculated band gaps in semiconducting and insulating materials. Within this own work, this can be seen with the calculated band gaps for the LLZO materials using PBEsol. Under most conditions, this functional is considered one of the best estimations for this class of material, but the results are 1-1.5eV below the experimental finding, a significant inaccuracy by scientific standards. The energies are described by continuous function known as energy bands in crystalline materials. Individual electrons in isolated molecules have their energies stored in discrete sets that take the form of molecular orbitals. Since most functionals struggle to distinguish metals from insulating materials (i.e. electrolytes), this subtle distinction in electronic states is usually the underlying cause for this error. The Kohn-Sham exchange-correlation functional upon which DFT is largely based suffers from this same issue.

Another issue arises with weak Van der Waals attractions, which are by nature long distance interactions that occur between small fluctuations in the electron density of one molecule and the electrons of another molecule responding slightly. This requires high-level wave-function based methods that are computationally expensive, so these interactions are often summed up. Because they can cause large effects in some systems, this can lead to rather significant energy deviations.

Finally, DFT struggles to compute systems larger than a few hundred atoms without access to highly developed code and powerful supercomputers. Obviously, this leads to a certain disconnect between real physical systems that involve billions or trillions of atoms within even a small physical. Therefore, the researcher needs to carefully understand the connection between these small systems and the much larger system to which it applies. This becomes even more difficult when attempting to calculate effects in motion or between inhomogenous surfaces.

3.10 Vienna Ab-initio Simulation Package (VASP)

The Vienna Ab-initio Simulation[49, 50, 51, 52] provided the framework for all DFT calculations to be performed in the current study. VASP utilizes periodic boundary conditions to create a simulation of an infinite lattice from a single supercell. Pseudopotentials and plane-wave basis sets for each atom are provided in the VASP library for use in calculations. The projector augmented wave (PAW)[51, 52] is the primary method used to carry out calculations. This is a frozen core approach, meaning the the inner core of orbitals use a set of empirical parameters to carry out calculations while the outer valence electrons' interacting forces are calculated at each step. The inner core electrons are only slightly involved in interatomic interactions, and the validity of the results has been confirmed when compared against all-electron calculations, which are far more computationally expensive. A combination of VASP functionality and VTST supplements provide the basis for NEB calcualations. VASP preserves symmetry considerations in order to speed up calculations and prevent undesired changes in symmetry. The other major theorems and techniques implemented in VASP have been treated in the previous sections of Chapter 3. Following is a brief description of the VASP algorithm, input, and output files.

Algorithm

1. Initialize geometry (POSCAR), pseudopotentials (POTCAR), k-point mesh (KPOINTS), and treat convergence conditions (INCAR). Unless otherwise stated, an electron density is automatically generated.

2. Self-consistent solution to the Kohn-Sham equations to reach the electronic convergence conditions (INCAR)

3. Calculates ionic forces and shifts position, volume, and shape as determined by the ISIF setting (INCAR)

4. Iteratively runs to ionic convergence

Files

POTCAR, POSCAR, KPOINTS, INCAR, and WAVECAR are the five primary input files considered when beginning a new calculation. OUTCAR, CHGCAR, CONTCAR, PROCAR, OSZICAR, and DOSCAR are the six primary output files produced, although others exist based on desired results.

- POTCAR specifies pseudopotentials for each ion contained in the POSCAR file. Must be in the same order as the POSCAR

- POSCAR defines starting geometry, lattice parameters, and ion positions

- KPOINTS defines the k-point mesh and k-point positions. Example pack meshes are the Gamma-centered and Monkhorst-pack[62]

- INCAR defines input paramaters for convergence. Important parameters include ENCUT (3.6.2), EDIFF (electronic convergence), EDIFFG (ionic

convergence) ISIF (Relaxation parameters), IBRION (determines ion update and movement), ISTART (Determines usage of WAVECAR and CHGCAR in start parameters), and GGA (exchange correlation functional

- WAVECAR contains data from a previous run for continuation
- OUTCAR gives detailed output of the VASP run
- CHGCAR This file contains the lattice vectors, atomic coordinates, the total charge density multiplied by the volume $\rho(r) * V_{cell}$ on the fine FFT-grid (NG(X,Y,Z)F), and the PAW one-center occupancies. Essentially the spatial charge density. CHGCAR can be used to restart VASP from an existing charge density. Written by LCHARG in the INCAR file
- DOSCAR contains the integrated DOS and DOS. Determined by ICHARG in the INCAR file
- CONTCAR contains updated ion positions and lattice parameters from the POSCAR
- PROCAR Contains the site-projected wavefunction character of each band or orbital
- OSZICAR Provides information about convergence speed, progress through each iteration, and the output energy for each iteration.

4 Computational Methodology

The following chapter contains the Computational methods used to perform the calculations. VASP.5.4.1[49, 50, 51, 52] using the Projector Augmented Wave (PAW)[63, 64] method with ultra-soft pseudopotentials[65, 66] and the generalized gradient approximation PBEsol[57], a functional designed to handle solids, were the primary tools utilized in calculations. Input files and critical scripts used in this study have been made available in the form of electronic supplementary information.

4.1 Structure

The current study focuses only on the primitive tetragonl unit cell. By relaxing only the ionic positions while keeping cell volume and shape fixed, the "dilute limit" can be observed. Using this scheme, defect-defect interactions and chemical expansion are consdered negligible at low concentrations[67]. To limit computational burden and the system complexity, it was decided to use the least number of atoms in a repeating cell necessary to recreate an endless lattice in infinite space, known as the primitive cell. The tetragonal structure obtained from the Materials Project[24] contains 96 atoms and has been labeled with the appropriate site labels to reflect the Wyckoff symmetry sites. The cell lattice parameters are 11.31Å for a=b=c. The coordination angles are $\alpha = \beta = 108.38°$and $\gamma = 111.682°$. The predicted band gap is 4.413 eV, cell density is $4.99 gcm^{-3}$, and cell volume is 1118.72 $^{\circ} A^3$. Potential interstitial sites were determined using the Voronoi Interstitial Finder script provided by Pymatgen[68]. V_{Li} sites were created by removing Li atoms at all of the available Li sites, as discussed further in Section 4.3. Vesta3.1.7[69] has been used for visualization, basic structural analysis, and generaton of the following images and structures for use with the VASP software[49, 50, 51, 52].

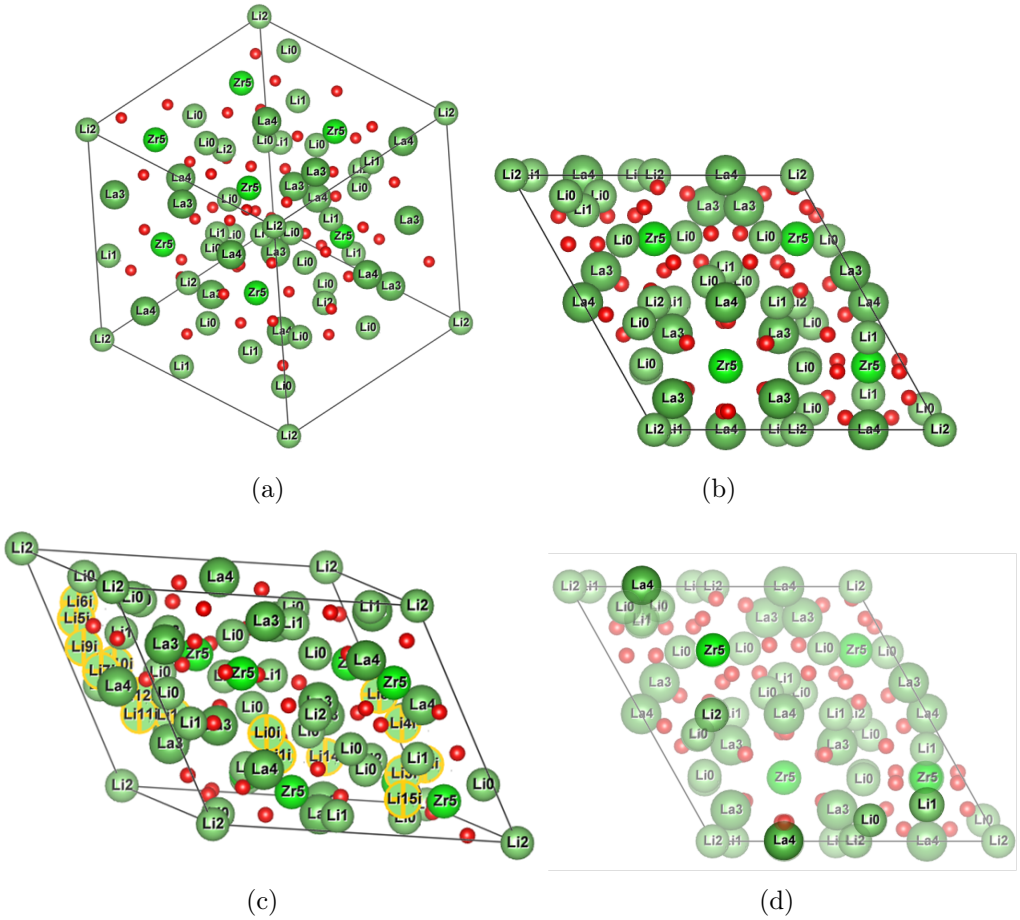

(a) (b)

(c) (d)

Figure 6: *a) LLZO Unit cell. b) LLZO top down view c) LLZO unit cell with all calculated inequivalent interstitial positions d) LLZO top down view with selected dopant positions*

4.2 Convergence Testing

In computational work, it is important to minimize the calculation time involved while still maintaining a reasonable degree of agreement with real world systems. Therefore, Convergence testing is vital in determining the proper K-point lattice as well as energy cutoff values needed to avoid excessive computational cost. Four series of tests were run: two series of 1x1x1 to 12x12x12 K-point mesh density for the Γ and Monhorst-Pack[62] mesh at a fixed energy cutoff of 350 eV and two more series over the 300-750 eV range at an interval of 50 eV with a fixed 2x2x2 Γ and Monkhorst-Pack mesh. The 2x2x2 Monkhorst-Pack mesh at 600 eV demonstrated the best balance between cost and convergence. There was only a slight improvement in cost and no significant difference in accuracy between the two mesh systems, as seen below.

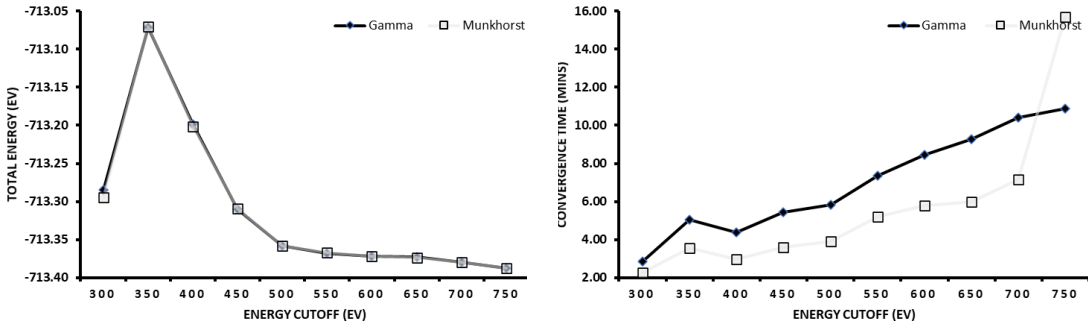

Figure 7: *Energy convergence for the LLZO system*

4.3 Defect Thermodynamics

All structures were derived from the original primitive LLZO structure, obtained from the Materials Project database[13, 24, 45, 70, 71]. Doping was done with Al, Mg, and Zn at each of the inequivalent wyckoff cation sites: Li2 (t), Li1 (O), Li0 (O), La4, La3, and Zr5. Li^+ ions were either removed to form negatively charged lithium vacancies or added at geometrically inequivalent sites in order to balance the charge structure. For example, Al^{3+} doped at a lithium site creates two lithium vacancies, at a lanthanum site it acts as a neutral defect, and at a Zr site it requires the addition of one interstitial Li ion. In order to determine the most favorable sites for doping and ion removal/addition, each dopant site was tested for Li^+ ions removed or added at a short and long distance as well as inequivalent wyckoff site combinations. This resulted in 100 structures that were narrowed down for further analysis according to the calculated value for the energy of formation. The ground state for each structure was calculated by relaxation of the ion positions with a fixed cell volume and shape using the Conjugate Gradient (CG) approximation . The approximate chemical potential was first calculated for each cationic oxide species (La_2O_3, Li_2O, MgO, ZnO, Al_2O_3, and ZrO_2) and O_2 from subsequent ground state energy calculations without corrections. PBE

approximation of the Li and molecular O_2 total energy is a well-known issue[72] and so values from experimental reference points[73] were compared against the generated data to ensure a reliable fit. First, a relaxation of O_2 in a large periodic box with dimensions of a=b=c= 25Å was performed with the intent that O_2 is able to move freely without periodic self-interaction. The acquired total energy O_2 was subtracted directly from the oxide total energy to calculate cationic species contribution. The total energies are assumed to be the chemical potential values that are subsequently used in Equation 4.1, denoted as μ_{cation}. These energies are compared against literature values in Table 2.

The energy minimizations were performed using a 2x2x2 Monkhorst-Pack k-mesh with an energy cutoff of 600eV and a relaxation of only cell positions. The pseudopotentials (PP) used implement the PAW method with the following valence electrons treated in the PP and the rest are taken into the frozen core approximation: Li_sv ($1s^2 2s^1$), La ([Xe]$6s^2 5d^1$), Zr_sv ([Kr]$4s^2 4p^6 5s^2 4d^2$), O ([He]$2s^2 2p^4$), Al ([Ne]$3s^2 3p^1$), Mg ([Ne]$3s^2$), and Zn ([Ar]$4s^2 3d^1 0$). The sv tag marks that the previous s and p orbitals are also considered in the valence band. Inserting the values for the cationic species' chemical potentials into the following equation:

$$E^f_{doped} = (E^0_{doped} - E^0_{stoich}) + n_{dopants} \times \mu_{0,dopant} + n_{Li} \times \mu_{0,Li} + n_{removed} \times \mu_{0,removed} \quad (4.1)$$

where μ is the chemical potential, n is the number of the specified species, E_f is the defect formation enthalpy/energy, $E^0_{doped} - E^0_{Stoich}$ is the difference in energy between the doped and pristine LLZO structures. Comparing the resulting values for the formation enthalpy, one structure was chosen for each dopant substituted at the most energetically favorable site for the three cationic species: Li, La, and Zr. This resulted in nine doped structures and one stoichiometric LLZO structure on which to perform DOS and NEB calculations. The full list along with associated formation enthalpies can be found in Table A1 Initial estimates for the chemical potentials for each ionic species were slightly deviant from experimental values, but within acceptable range. The formation enthalpy equation excludes more computationally expensive methods, such as that described in Moradabadi and Kaghazchi[35], which takes into account valence and conduction band density of states in relation to a fermi-dirac distribution. This method also requires highly accurate results relative to real-world conditions from the DOS calculations that were that were not necessary for the current study. However, formation enthalpies in this study are adequate to compare internally to determine relative suitability and the values are within an acceptable range to experimental values to prove their validity.

4.4 Density of States

The density of states (DoS) calculations quantifies available electronic states for each of the orbital energy levels for each ion in the lattice, describing the electronic structure in the process. This can also be used to define the electronic conductivity and magnetic properties. The calculation was performed in two main steps. First, a static, self consistent field (SCF) calculation generated a charge density field

in a single ionic step with fixed parameters for the cell and atoms. This field is then used in the non-SCF calculation to keep a fixed charge density so that each k-point can be treated independently. The DoS data can then be used to produce the value of the band gap and occupied states by each species. The defect states are of particular interest as they can potentially provide information on the location of deep electron trapping at delocalized holes within oxygen sites neighboring the dopant site. As discussed in section 3.9, most standard DFT functionals, such as GGA and LDA, underestimate the band gap in insulating materials. Hybrid functionals like HSE06 better approximate the band gap in crystalline solid insulators compared to these standard functionals due to the well-known self interaction error and incorrect charge density localisation[74]. The hybrid functionals and further corrections yield highly accurate band gaps at the expense of high computation costs[75, 35]. The PBEsol-GGA functional should provide a reasonable estimation of the location of the defect states and other major shifts in the electronic structure at a fraction of the computational cost.

The DOS was sampled over a 2x2x2 k-point Monkhorst-Pack grid with an energy cutoff of 600 eV. The input files can be found in the electronic supplementary information. The expanded band structure of LLZO is quite dense as can be seen in Figure 8 below and requires more intensive calculations of eigenvalues along high-symmetry pathways. This data provides very little additional information that could be used in this study so it was decided to forego these calculations in favor of the simplified DOS.

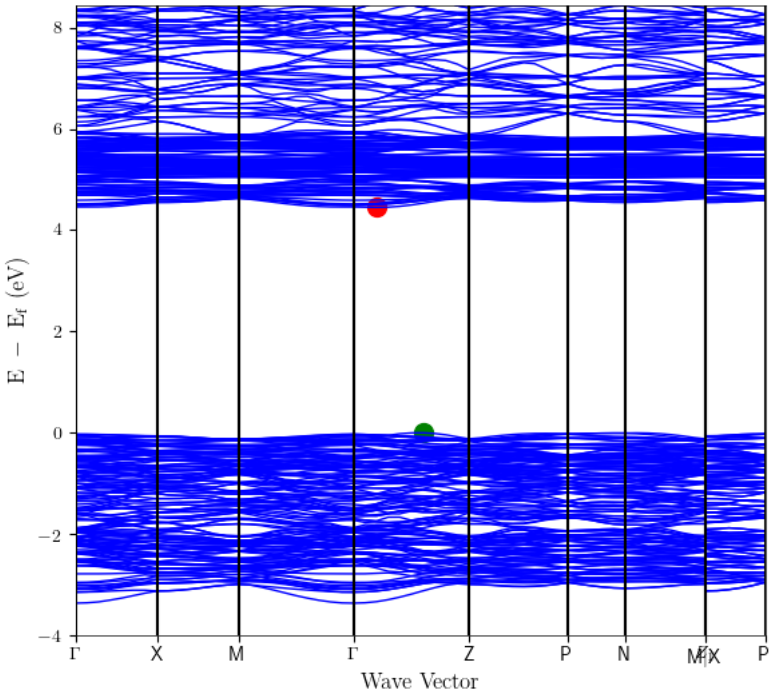

Figure 8: *Band structure data and figure provided by The Materials Project[24]*

4.5 Nudged Elastic Band Calculations

Migration paths were selected on the criteria that they pass contiguously from one supercell to the next via single-ion hopping. While concerted migration has already been addressed as the primary mechanism for lithium migration in the tetragonal phase, this mechanism is difficult to model accurately. This is particularly true within the NEB framework, which fails to account for the dynamic hopping environment of all possible Li/Li vacancies. Previous studies have confirmed the presence of this mechanism using advanced molecular dynamics (MD)[25, 29] or machine learning[28] techniques, but this is outside the scope of this study. Relative energy barriers will provide the necessary data.

The migration pathways in this study are determined by a method developed within Pymatgen[68]. Using geometric considerations of inequivalent sites, sample hops are generated for all geometrically possible migration paths. Using the generated structures, continuous pathways through the lattice were determined, meaning that the lithium could theoretically transport along these pathways across an infinite sized lattice without interruptions. Figure 9 presents all the generated lithium vacancy hops possible for the symmetrized lattice and the three continuous lithium migration pathways in the primitive tetragonal structure that were used for this study. It was important to take into account the initial structures that were used to generate the lithium ion hopping. The initial hop was always made from an occupied Li site into the lowest energy vacancy in the structure, as determined in Section 5.1.

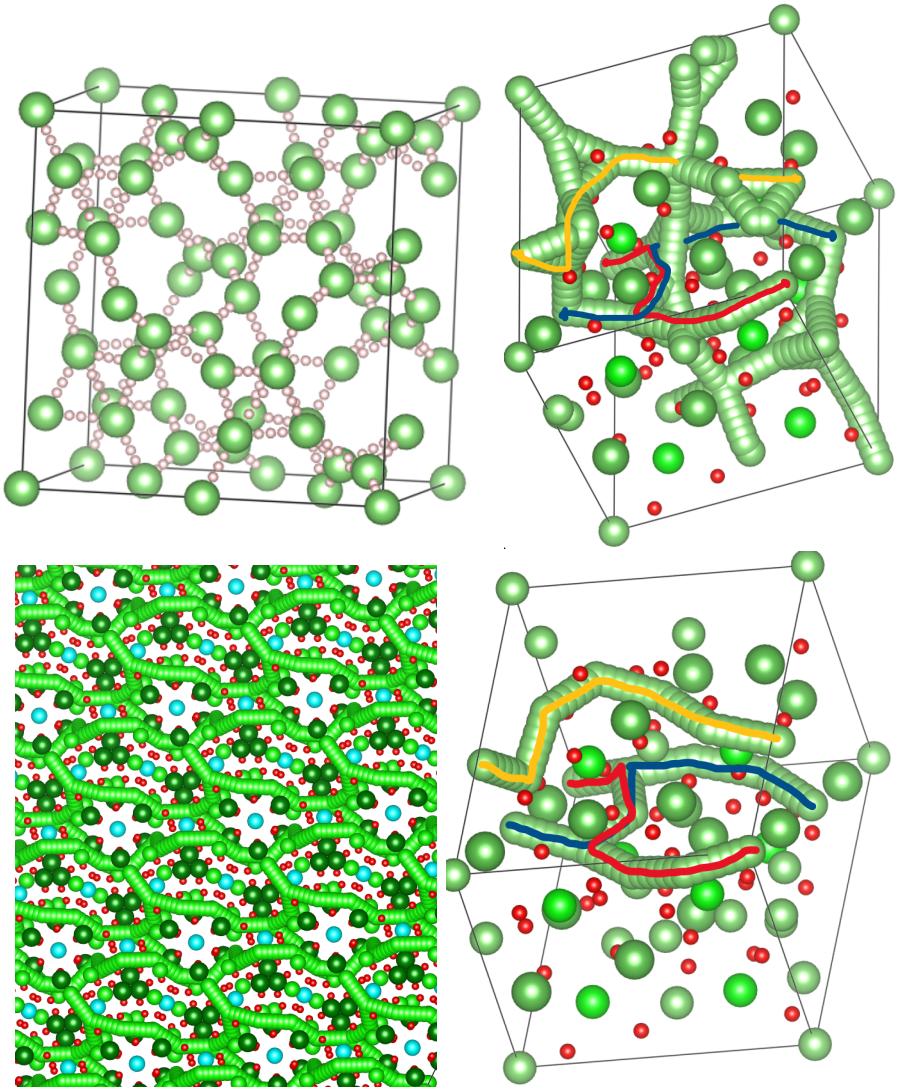

Figure 9: *(top left) All possible Lithium hops in the symmetrized LLZO cell. (top right) The three shortest selected continuous migration pathways shown alongside all possible paths. (bottom left) Continuous pathways through an extended lattice (bottom right) selected migration pathways isolated*

Five to seven images were produced per hop. The script used to generate these images and their associated structures have been included in the supplementary information. Each minimum-distance, continuous migration pathway constisted of six inequivalent hops (except in the pristine LLZO system) which were calculated individually. The total Lithium migration path energies were then to be pieced together to find the total migration barrier across the lattice for each dopant/site combination. Several methods were attempted to calculate the desired migration barriers, including both standard NEB and the climbing-image method developed by VTST[76]. At the time of writing, no method or set of input parameters yielded desirable or accurate results within a reasonable convergence time. All calculations took place within the VASP software. The migration barrier energy is synonymous with the activation energy (E_A), from which the diffusion coefficient can be calculated using a simplified Arrhenius expression as follows:

$$D_{Li} = D_0 exp(\frac{-E_A}{k_B T}) \tag{4.2}$$

where D_0 is the pre-exponential factor, k_B is Boltzmann's constant, and T is temperature. The D_{Li} term takes into account the jump factor and frequency for this system, with some variation depending on the method used.

One such intensive method developed is to determine the pre-factor by the explicit inclusion of the vibrational dynamics of the system such that the migrating species is present at both the equilibrium position and the saddle point[77]. This method was developed from two sets of work that form the basis of transition state theory. First, Vineyard's formula[78] is used to define the prefactor by the set of vibrational frequencies for the equilibrium (v_i) and the saddle point (v_j) configurations. This is represented by the formula $D_0 = \prod_{i=1}^{N} v_i / \prod_{j=1}^{N-1} v_j$. The second part of this method is devised from the work of Kurpick et. al.[79, 80, 81, 82]. They devise a method for the prefactor calculations through evaluation of changes in vibrational contributions to the free energy of the system, validated within the limits of Transition State Theory[83]. The number of equivalent jumps n is the product of the time period and the hopping rate Γ for thermally activated diffusion. This is defined as $\Gamma = \frac{k_B T}{h} exp(\frac{-\Delta F}{k_B T})$. Thus, the prefactor is redefined with constants for jump distance d and dimensionality of the motion α as

$$D_0(T) = \frac{k_B T}{h} \frac{n d^2}{2\alpha} exp(\frac{\Delta S_{vib}}{k_B}) exp(\frac{-\Delta U_{vib}}{k_B T}) \tag{4.3}$$

where S_vib is the vibrational entropy and U_vib is the vibrational potential energy. This method requires the calculation of several extraneous factors, such as the jump frequency and vibrational entropy, which would make it further necessary to calculate phonons in the initial and saddle points of an extremely large sample cell.

D_{Li} can also be estimated using the RMSD method[47], which requires the use of kinetic Monte Carlo (kMC). This is a method of molecular dynamics that

can define the evolution in time of the set of Li atoms as they diffuse through the lattice. However, any of these methods takes a considerable amount of time that is outside the scope of this project. For this purpose, an estimation of the prefactor is adequate.

The prefactor used in this study is estimated at $2 * 10^{-4} cm^2 S^{-1}$, which was determined for a Nb-doped LLZO system[84]. While this prefactor is not completely accurate to the systems in this study, the migration barrier (E_A) in equation 4.2 will largely dominate the resulting diffusion term and provide a decent estimate. Using the obtained Diffusion coefficient, the ionic conductivity (σ) can be determined by the Nernst-Einstein relation.

$$\sigma = \frac{q^2\, c}{k_B\, T} \times D_{Li} \tag{4.4}$$

The term c refers to lithium concentration, k_B is the Boltzmann constant, and q is the charge of the Li charge carrier. This equation can be iterated over an estimated range of concentration (1×10^{-14}cm^{-3}-1×10^{-20}cm^{-3}) and temperature (200K -1000K) to generate a temperature and concentration dependent mapping of the diffusion properties in the lattice. These rough estimates will allow a quantitative comparison between the structures discussed within this study.

5 Results

This chapter contains the results from minimization/relaxation of the primitive structure for each of the selected structures as well as the process for selecting the final ten structures on which to conduct further analysis. This extended analysis includes DOS and CI-NEB calculations to determine the energetic migration barriers across the LLZO lattice. All calculations were done with a fixed volume and shape in order to retain constant lattice parameters and cell energetics across all configurations. This allows for a measured comparison of ion displacement and lattice distortion associated with dopant choice and vacancy site location.

5.1 Defect Thermodynamics

In order to calculate the formation energy E_f as seen in eq.4.1 for each doped structure, the ground state Fermi energy for each oxide ion needs to be determined. Elemental O_2 is placed in a supercell with dimensions a = b = c =25 Å and allowed to relax only the ionic positions. The calculated value per atom can then be subtracted from the total energy for each of the oxides to find the cationic contribution. The results for these energies can be found in Table 2 below. These values show reasonably acceptable agreement with physical values and are reasonably confirmed by calculations using the Pymatgen[68] software suite.

Table 2: *Calculated and reference experimental values of the chemical potentials for individual ions*

Compound	O_2	MgO	ZnO	Li_2O	La_2O_3	ZrO_2	Al_2O_3
μ **(eV)**	-5.14	-7.37	-9.29	-4.81	-14.19	-19.73	-11.96
Ref. μ **[73]**	-4.92	-7.13	-9.39	-4.72	-14.29	-19.43	-11.63

Following from this, the ground state energies were calculated for 100 different structures that offer a representative landscape of the direct-charge compensation model for the three dopant oxides relative to the doping site and the respective removed vacancy or added interstitial sites. The full data sets of the energies and formation energies of these structures can be found in Appendix B. The nomenclature for vacancy structures follows this formulation; $M_{Li}\_V_{Li[sitenumber]}$(position number). The position numbers are arbitrarily generated for internal use with each site being linked to a number range: Li0 (xiii - xxviii), Li1 (v - xii), and Li2 (i - iv). i.e. a Mg ion substituted at the Li2 site with a vacancy at the fifteenth Li position (a Li0 site), would appear as $Mg_{Li2}\_V_{Li0}$(xv). The interstitial structures followed a similar formula with positions ranging from 0 - xv; M_{Li}+[L_i(position number)]. For example, a Zn atom doped at a La3 site with interstitial at position number four would be referred to as Zn_{La3}+Li_i(iv).

The ten target structures in Table A1 were determined from the lowest calculated formation energies for each dopant-site combination. For doping at the lithium site, Table A3 shows that the substitution of the dopant species at the

tetragonal Li2 site is energetically favored for each dopant species, so further substitutions took place at the Li2 site. The creation of one (Mg and Zn) or two (Al) vacancies at the Li0 site proved to be the most stable configuration utilized for further study. Creation of a vacancy at either a Li0 or Li1 site is energetically favored over a Li2 vacancy by at least 1eV, which is in agreement with previous studies[14] and can be seen as the three outliers in Figure 10. In order to determine the relation between vacancy distance relative to the dopant site, displacement, and formation energy of the associated structures, Table A2 was compiled. Zinc was chosen to test this relation since only a single vacancy is needed to balance the charge, limiting the required number of structures to determine the optimal vacancy position. These results show that energy and displacement and formation enthalpy tends to increase as distance of the vacancy site from the doping site increases. This trend is expected as the negative energy associated with V'_{Li} is offset by close proximity to the increase in charge experienced at the substitution site. Some clear exceptions can be seen, such as with V_{Li0}(xxiv), V_{Li0}(xxvi), V_{Li0}(xvii), and V_{Li0}(xxiii), presented in Figure 10. This is most likely a result of interacting ions between these sites and the dopant site. This slight difference in environment may be the cause of these minimal shifts in energy. A further discussion of the energetic environment relative to displacement is presented in 6.2 The calculations in Table A3 were repeated with the lowest energy positions relative to these conclusions to ensure the same results, which is the data that is now presented. For $Al_{Li2}\_V_{Li0}\_V_{Li0}$, a separate test had to be conducted with a pairing of two close vacancies (V_{Li0}(xvi) and V_{Li0}(xvii)), close and mid vacancies (V_{Li0}(xvi) and V_{Li1}(x)), and close and far vacancies (V_{Li0}(xvi) and V_{Li0}(xxiv)). The two close vacancies resulted in the lowest energy conformation.

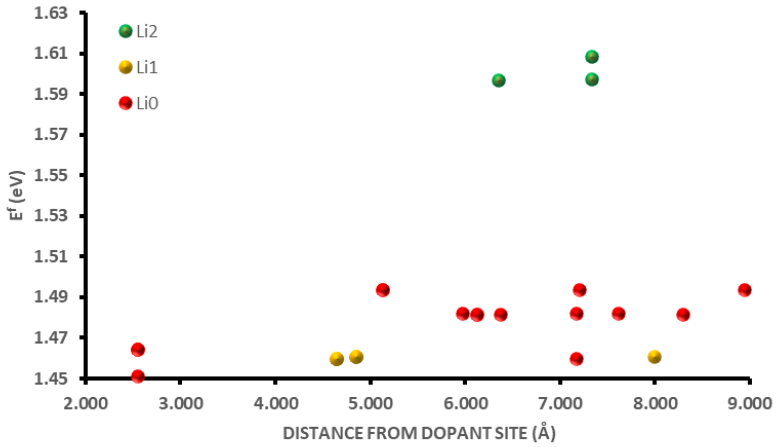

Figure 10: *The vacancy formation enthalpy E^f as a function of distance for the $Zn_{Li2}\_V_{Li}$ structures*

Similar tests were performed for the interstitial sites relative to the Zn4 site, as seen in Table A6 and Figure 11. Although the La3 site (Table A4) was eventually determined to be lower in energy, the La3 and La4 testing positions were quite

close and expected to yield similar results. The same conclusions hold true for the interstitial sites. These sites yield a higher formation energy for the sole reason that more ions are added to the system as opposed to being removed, which inherently increases the energy of the system using 4.1. However, higher lithium content is likely to increase the ionic conductivity, as will be discussed in further detail in Chapter 6. Mg and Zn are more energetically favorable in the La3 site, with the former showing slightly more preference due to its lower potential. Al is energetically favorable in the Zn5 site, which is not in agreement with previous findings that predict the Mg site to favor this site[23]. There is a more pronounced trend towards higher energy than with the vacancy structures as the interstitial is placed farther from the dopant site, as seen in Figure 11. This indicates a coulombic attraction between the dopant and the interstitial site as expected. However, the lowest energy interstitial structure is still higher than the highest energy V_{Li} formation enthalpy, so a preference towards vacancy formation might be expected.

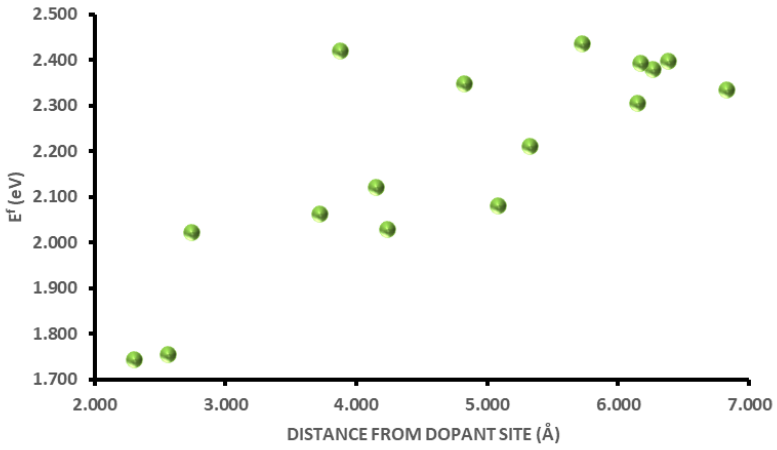

Figure 11: *The interstitial formation enthalpy E^f as a function of distance for the Zn_{La4}+Li_i structures*

5.2 Displacement

The displacement data presented in this section refers to two observed types of change in the relaxed structures. The first is the vector sum, which defines the overall change in distance, measured in Angstroms, of all atoms from their respective original positions to their updated positions in the relaxed cell. As mentioned in the previous section, a correlation can be seen between the value of the vector displacement and the resulting formation energy. In this section, it will be shown that it is not only the overall sum, but the displacement of particular atoms and to what degree they shift position that affects the system energetics. The second point of interest is the change in bond length for oxygen atoms bonded to the dopant site. This is of particular interest since these atoms may play a role in

lowering the formation enthalpy of the V'_{Li} site and creating the necessary disorder in the crystal lattice to stabilize the cubic phase. Scripts from the UT Austin Henkelman *Vasp Transition State Tools* (VTST)[76] have been used to compile the displacement data generated and Vesta[69] to analyze the bond lengths and polyhedral volumes.

5.2.1 Vector Displacement

There appears to be a direct relation between the displacement and the formation energy for each structure. To elucidate this relationship and what structural changes may be responsible, the individual atoms have been separated by distance relative to the dopant site against displacement as seen in Figure 12. This first figure is the lowest energy conformation of the Zn_{Li} structures that will be utilized in this section and the discussion in Section 6.2 to determine the relationship between displacement and the proximity of perturbations, such as V_{Li} and Li_i relative to the dopant substitution site. In particular, if the initial assumption holds true that the formation enthalpy will increase with total displacement, then these graphs are key to understanding where the lattice distortions take place, to which atoms, and to what degree. The full collection of data is presented in Appendix B.2 for the ten target structures in Table A1. This set represent each of the three dopants at the most energetically favorable Li, La, and Zr sites as well as the stoichiometric LLZO structure to serve as a reference point. For the relevant discussion, a series of Zn-doped structures at the Li2 and Zr4 site were calculated with each possible vacancy site and interstitial site, respectively. The full list with related formation energies, vacancy distance, and the vector displacement are presented in Table A2 and Table A6.

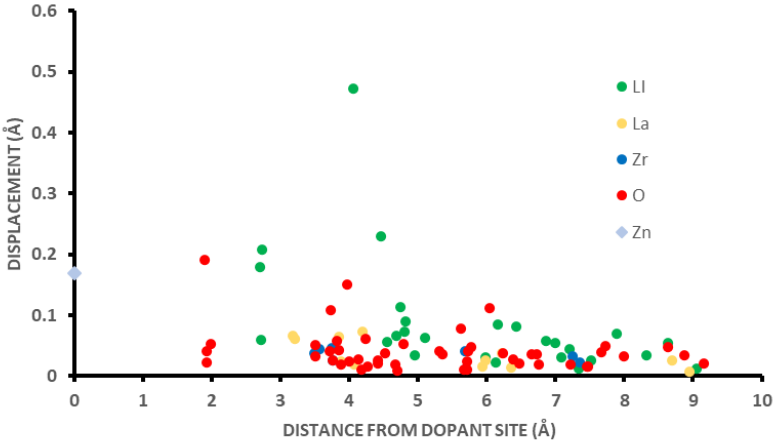

Figure 12: *Displacement per individual atom in the $Zn_{Li2}\_V_{Li0}$ structure by distance from the substitution site*

Figure 13 compares the lowest energy structure for vacancy formation at the Li0, Li1, and Li2 sites in the Zn-doped system. A fifth order polynomial is used to fit the data and show the relative displacement trend across distance for each

structure. Based on the formation enthalpies presented in Figure 10 and Table A3, $Zn_{Li2}\_V_{Li2}$ has a much higher formation enthalpy than vacancies generated at the Li1 and Li0 sites. Figure 13 indicates that the cause of this trend is high displacement in ions farther from the dopant site, depicted by the large displacement curve for the V_{Li2} (green) structure vs the V_{Li1} (yellow) and V_{Li0} (red) structures. This is also due to the important structural role that the occupied tetrahedral Li2 (8a) plays with the unoccupied tetrahedral vacancies (16e), that also act to stabilize the site.

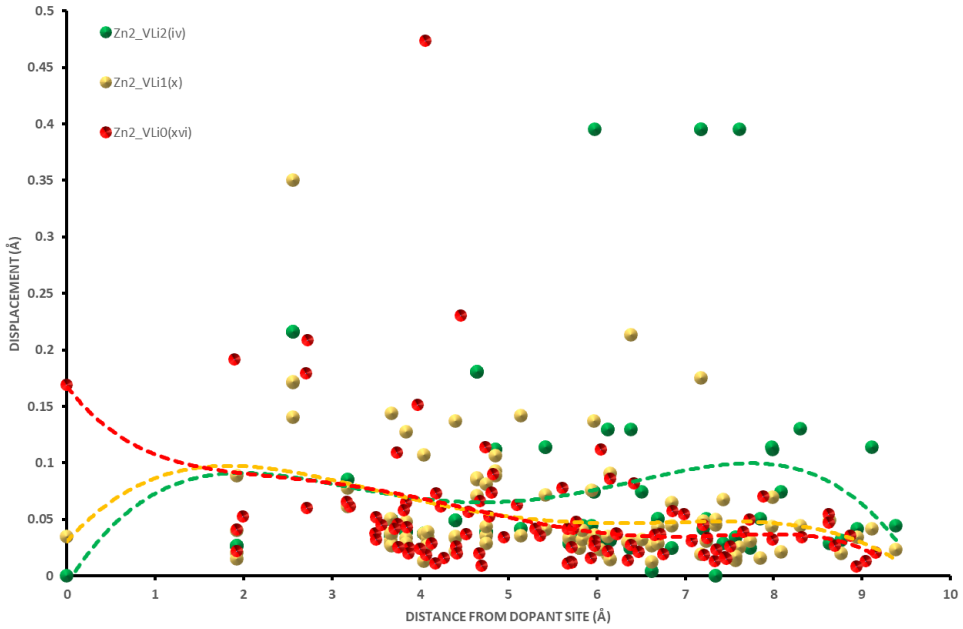

Figure 13: *A comparison of atom distance from the doping site vs displacement of the three lowest energy conformations for vacancies in the Li0, Li1, and Li2 sites*

The trends are not readily apparent, but this shows that oxygen and lithium displacement are highest closer to the dopant and vacancy site, which is to be expected as these atoms most directly interact with these sites. These atoms would most acutely experience the charge imbalance in the resulting structure and relax their positions to accommodate this change. However, a further analysis by vacancy site and atom type may be able to elucidate what atoms affect the formation energy to the greatest extent. A base assumption that displacement alone is responsible for the formation energy is inadequate and inaccurate in describing the effects that higher charged ions such as La and Zr may have. As such, a displacement factor f_{atom} was calculated with the following rationale $f_{atom} = (d_{atom}/\sum d_{atom}$. This value thereby relates magnitude of a particular atom's displacement on the overall structure's formation energy. This value is only a rough estimate which does not account for electrostatic interactions, only raw displacement lattice distortion values for each atom. Table A7 presents the calculated f_{atom} for the total Li, La, Zr, O, and Zn site displacement in an effort

to further determine the structural changes related to each vacancy's formation energies. Figure 14 shows this relation for each atom's total displacement factor to formation energy. Similarly, Figure 15 breaks down the individual Li sites. The two figures display how Li and oxygen displacement, particularly at the Li0 site, has the greatest proportional affect on the displacement, and thus, the formation energy. Similar effects occur in the Mg and Al doped structures, presented in Appendix B.2. This confirms the high amount of lithium disorder as a result of doping that may make these stabilize the cubic phase. It also explains the high formation energy associated with vacancy formation at the Li2 site, since these seem to be fairly stable to displacement. Additionally, it disproves the original assumption that La and Zr displacement were primarily responsible for the high formation energies. Instead, it would seem that a lower displacement magnitude of these two atoms implies a higher formation energy since they would perhaps interact to a lower degree with the defect sites.

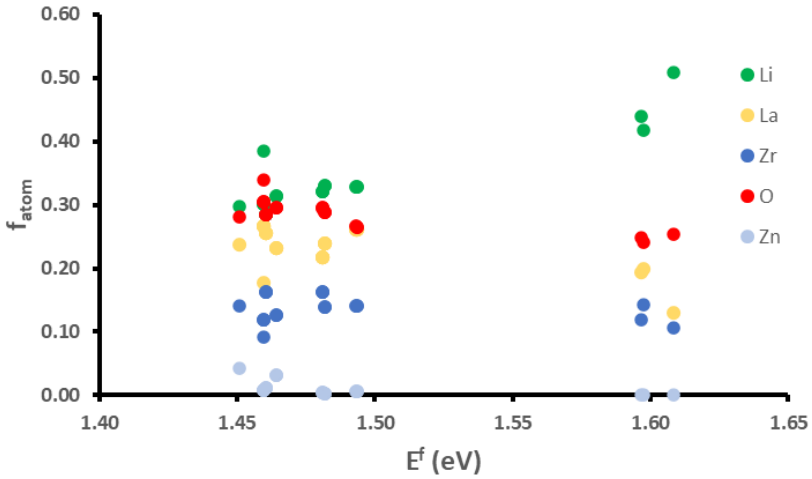

Figure 14: *Displacement factor by atom type at each of the 27 $Zn_{Li2}\_V_{Li}$ structure's respective formation energy*

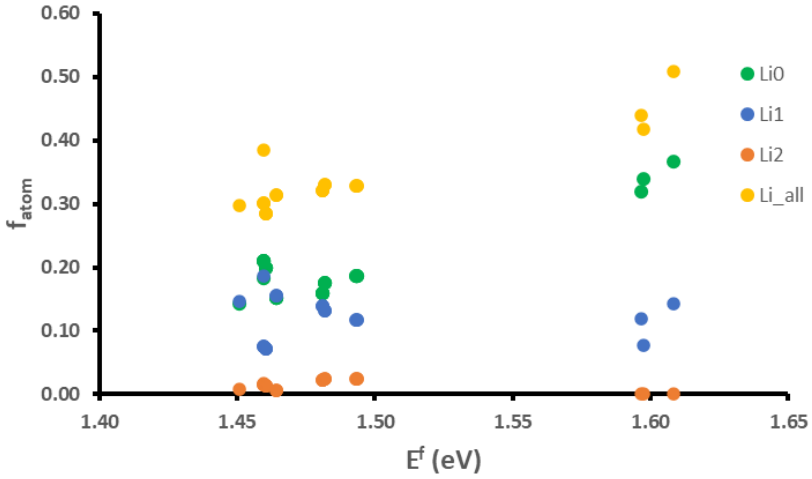

Figure 15: *Displacement factor for each Li site in the 27 $Zn_{Li2}\_V_{Li}$ structures*

The same calculations were repeated for Zn-doping at the La4 site with all sixteen possible interstitial positions. These are presented in Figure 17, Figure 18, and Table A8. The displacement by individual atom is provided in Figure 16 The interstitial contributes a large amount of energy to the system that creates a much larger displacement at all atomic positions in the structure, particularly those closest to the interposed interstitial site. As such, the overall displacement factor is not as greatly overwhelmed by the lithium contribution. This behavior is to be expected as more energy is introduced to the system with the addition of atoms as opposed to their removal. This is reflected in the significantly higher formation energies.

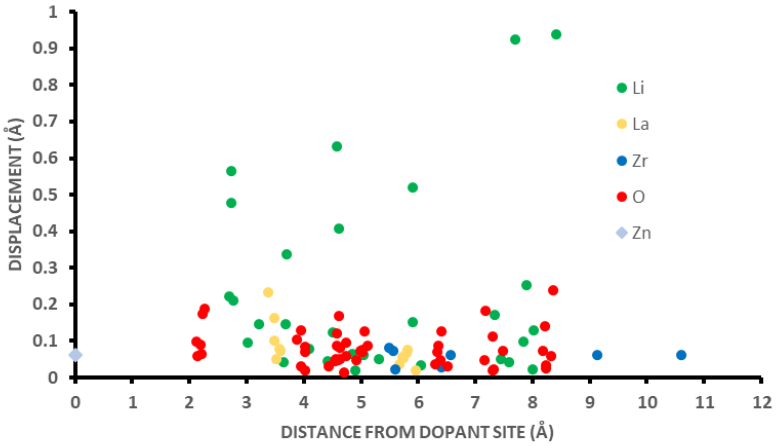

Figure 16: *Displacement per individual atom in the Zn_{La4}+$Li_i(0)$ structure by distance from the substitution site*

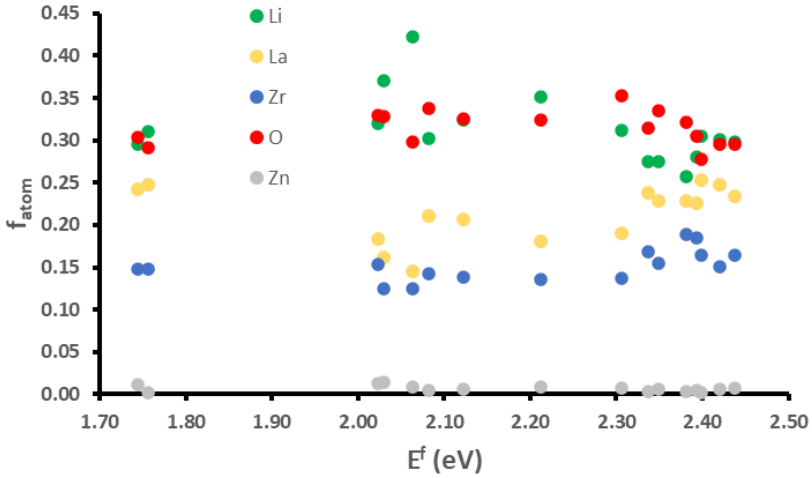

Figure 17: *Displacement factor by atom type at each of the 16 Zn_{Li2}+Li_i structures' respective formation energy*

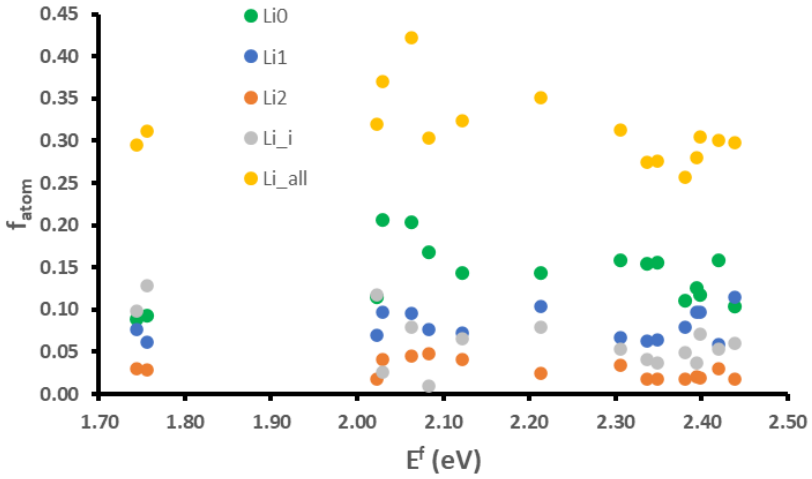

Figure 18: *Displacement factor for each Li site in the 16 Zn_{Li2}+Li_i structures*

The same calculations were applied to doping at the Zr5 site, but this did not add any significant data to the study and has thus been excluded. In looking at Table A5, it is critical to notice that different interstitial positions were selected for the final structures ($Li_i(x)$ and $Li_i(xv)$), primarily due to distance from the doping site, which has already been considered in the figures and data presented.

5.2.2 Dopant Site Oxygen Bonding

The LLZO lattice, as with most garnet type structures, is composed of cations bonded to oxygen anions which form the backbone of the crystal structure. By analyzing the displacement of oxygen bonding at dopant sites in comparison to their undoped counterparts, it may grant some insight to the structural changes that occur near the doping site. How might this affect the lithium migration? As stated previously higher valence dopants such as $Al_3{}^+$ may hinder Li-mobility by effectively blocking possible migration pathways[40]. This could potentially be a result of unfavorable O-bond breaking or contraction/expansion of the lattice in these positions. Alternatively the structural changes could be preferable and lend to the lithium disordering in the structure that aids in the cubic phase transition. Figure 19 shows the relative bond lengths and even breaking in the case of La-site doping. When comparing the results for the displacement index in Table 4 to the formation energies in Table A1, a close correlation can be seen. This concept will be discussed in more detail in 6.2.

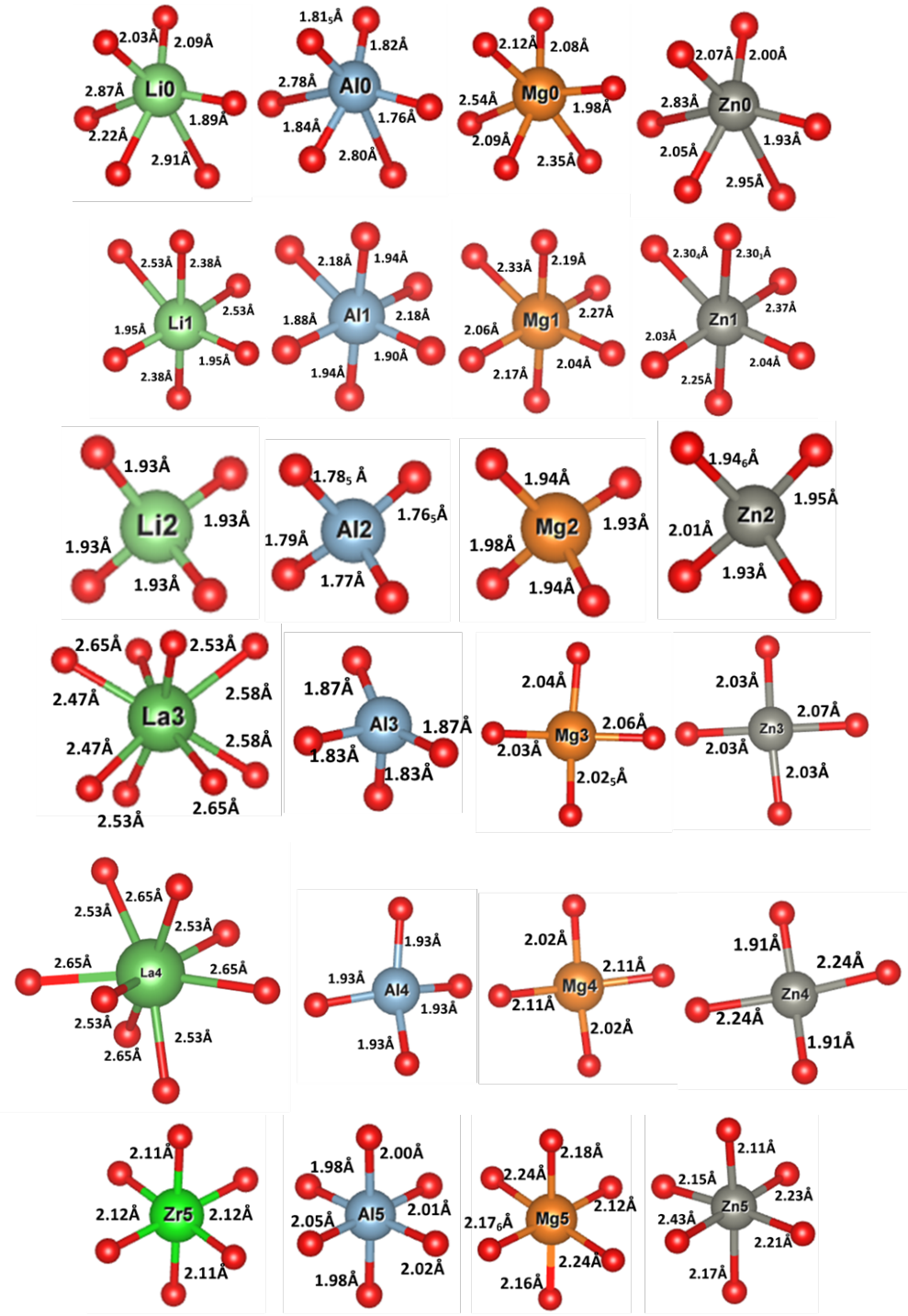

Figure 19: *Dopants at each of the target dopant sites after relaxation in the most energetically favorable conformations, which can be found in AppendixB*

A displacement index Z_{eff} is used here as a normalized sum of the weight of each bond length relative to the original dopant site. A value of 1 implies that oxygen has no displacement from the replaced ion, $Z_{eff} > 1$ shows bond stretching, and $Z_{eff} < 1$ shows shorter bonding to the new ion.

$$Z_{eff} = \frac{1}{i} \sum_{i=1}^{i} \frac{d_i}{d_{site,avg}} \tag{5.1}$$

where i is the number of dopant-O bonds present at the doped site, d_i is the bond distance between the dopant and a specific oxygen atom, $d_{site,avg}$ is the avg site bond length, and Z_{eff} is the effective displacement index. Absolute deviation from the non-displaced ion (Δ) can be calculated using the following

$$\Delta = \sqrt{(1 - Z_{eff})^2} \tag{5.2}$$

Table 3

Dopant Site	d_{avg} (Å)	$V_{Polyhedral}$ (Å^3)	$d_{avg,cubic}$	Z_{eff}	Δ
Li0	2.33	15.17	–	1.00	0.0
Al0	1.81	2.52	–	0.78	0.63
Mg0	2.20	13.35	–	0.94	0.34
Zn0	2.01	3.37	–	0.86	0.51
Li1	2.29	15.02	2.10	1.00	0.0
Al1	2.00	10.38	–	0.87	0.49
Mg1	2.18	13.31	–	0.95	0.31
Zn1	2.22	13.97	–	0.97	0.24
Li2	1.93	3.70	1.92	1.00	0.00
Al2	1.78	2.85	–	0.92	0.92
Mg2	1.95	3.71	–	1.01	0.14
Zn2	1.96	3.79	–	1.02	0.20
La3	2.56	28.49	2.55	1.00	0.00
Al3	1.85	2.79	–	0.72	0.69
Mg3	2.04	1.14	–	0.80	0.60
Zn3	2.04	0.83	–	0.80	0.60
La4	2.59	29.53	–	1.00	0.00
Al4	1.93	2.25	–	0.75	0.66
Mg4	2.07	1.01	–	0.80	0.60
Zn4	2.08	0.90	–	0.80	0.60
Zr5	2.12	12.58	2.10	1.00	0.00
Al5	2.01	10.71	–	0.95	0.31
Mg5	2.19	13.76	–	1.03	0.25
Zn5	2.22	14.33	–	1.05	0.32

The majority of sites experience a contraction in O-bond lengths. The primary driver behind this is the difference in valency and electronegativity between the

original ion and the dopant. The +2 charge difference that results from Al bonding at a lithium site would have a greater effect than the +1 charge difference created from Mg or Zn. Further differences are likely due to the electronegativity of the ions, with Al, Zn, and Mg having relatively high values of 1.61, 1.65, and 1.31, respectively. For comparison, Li has an electronegativity of 0.98. While Al and La have similar ionic radii and valence charge, Al has a higher electronegativity than La (1.1). This shortens the bond length of the four tighter bonded oxygen atoms, which likely creates a negative potential that breaks the weaker covalent bonds of the outer four oxygens as seen in Figure 19. Zr, on the other hand, has an electonegative charge of 1.33, which may explain the relative stability of the O-bonds in the doped structures.

5.3 Density of States Calculations

The density of states data collected here is not heavily used, such as in calculating the formation energy or deeper studies into the band structure and electrochemical stability. However, it is used to compare the band gaps of the lowest energy conformation structures for each of the three dopants and provide some insight into relative suitability of each site. The electrochemical window of LLZO has been experimentally measured primarily utilizing electrochemical cycling and impedance measurements to be between 5.8 and 6.1eV[6]. A wide range of functionals and correction methods can be used to estimate the band gap through first-principles DFT calculations. Thompson et. al. calculates these values in a range from 5.5 to 6.4eV[75]. HSE06 is regarded as the most reliable and physically accurate for insulating materials at a value 5.8eV[35, 75]. In this study, PBEsol is used for cost constraints and ease of analysis. A value of 4.28 $\pm 0.1eV$ is reported in the band gap for the undoped LLZO system, with the full range of values for each structure reported in Table 4. The indirect band gap is calculated from the difference in the lowest occupied orbital in the conduction band (right) and the highest occupied orbital in the valence band (left) The full DOS is presented below for undoped LLZO in Figure 20 and the data for each conformation in **??** in appendix B.3.

Table 4: *Calculated Band Gaps for the doped and undoped LLZO system*

Structure	**Bandgap** ($\pm 0.1eV$)
LLZO	4.280
$Al_{Li2}\_V_{Li0}\_V_{Li0}$	3.607
$Zn_{Li2}\_V_{Li0}$	4.320
$Mg_{Li2}\_V_{Li0}$	4.343
Al_{La3}	4.115
Zn_{La3}+Li_i**(0)**	3.521
Mg_{La3}+Li_i**(0)**	4.145
Al_{Zr5}+Li_i**(x)**	4.155
Zn_{Zr5}+Li_i**(x)**+Li_i**(xv)**	3.888
Mg_{Zr5}+Li_i**(x)**+Li_i**(xv)**	4.135

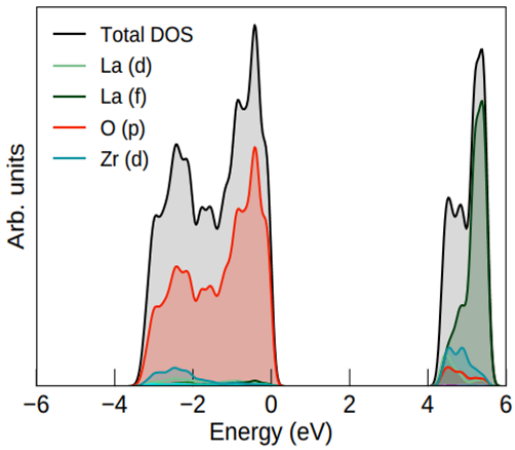

The Sumo Python toolkit[85] was used to produce all DOS figures.

Figure 20: *The Density of States for Stoichiometric LLZO*

The electronic structure for LLZO is characterized by the overwhelming influence oxygen in the VB, due to it's almost fully occupied p orbitals, resulting from the formation of bonds with nearby cations. The Li atoms only weakly bond to nearby oxygen atoms, which is why their presence is too small to appear in the DOS (<3% of total states). La ([Xe]$5d^1 6s^2$) has only partially filled d and f orbitals, so with 24 mostly unoccupied La orbitals, these orbitals dominate the conduction band at the highest energies with only a slight influence in the valence band. Similarly, Zr's d orbitals are mostly unoccupied, although much lower in energy than La's f-orbitals. As such, Zr energy states are mostly present in the CB, with some occupied orbitals resting below -2 eV.

The defect states are of particular interest as they give insight to the electronic structural changes that enact lattice distortion and Li disordering. It is expected that deep or shallow defect oxygen states will arise in the band gap as a result of delocalized electrons being trapped at vacancy or oxygen sites. A full discussion of these forbidden states can be found in Section 6.3. Despite these expectations, there are no visible gap states in any of the final tested structures. Although some shifting of the fermi level appears to occur with the associated figures below, this is only a result of the post-processing smearing applied to smooth the jagged data lines. The influence of the dopants can primarily be seen with distinct energy states in the adjacent oxygen states, as well as the Li and Zr states to a lesser degree. The most prevalent of these states appear within the valence band, lower in energy than the bulk of the occupied states, but some occupy states close to the valence band maximum (VBM) as well. Some smaller defect states can also be seen in the conduction band close to the conduction band minimum (CBM). The peaks most likely correlate to the influence that the dopant has on oxygens bound to the substituted site, which explains the more pronounced effect in the valence band. The number of peaks is the same as the number of bonds seen in each of the site substitutions in Figure 19 Besides these peaks, there is a low density throughout the heavily occupied region of the VB and the CB. Below, Figure 21,

in Figure 22, and Figure 23 show the defect effect by separating and enhancing the image size for the defect orbital peaks.

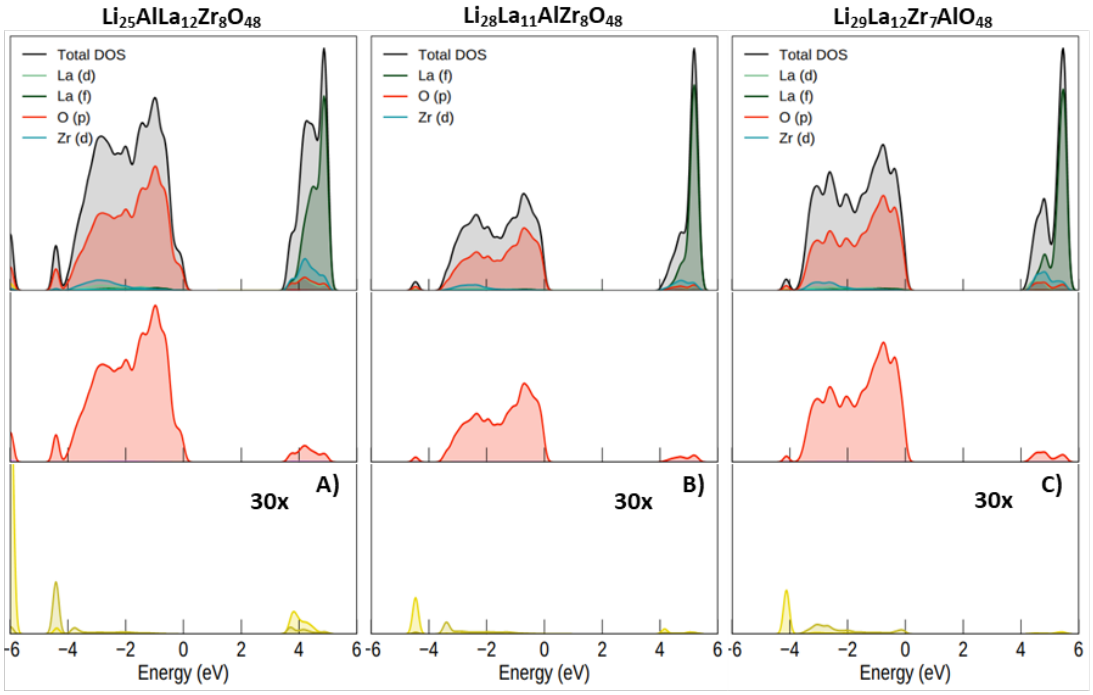

Figure 21: *The Density of States separated by atom for the Al-doped LLZO at the Li2, Las3, and Zr5 sites*

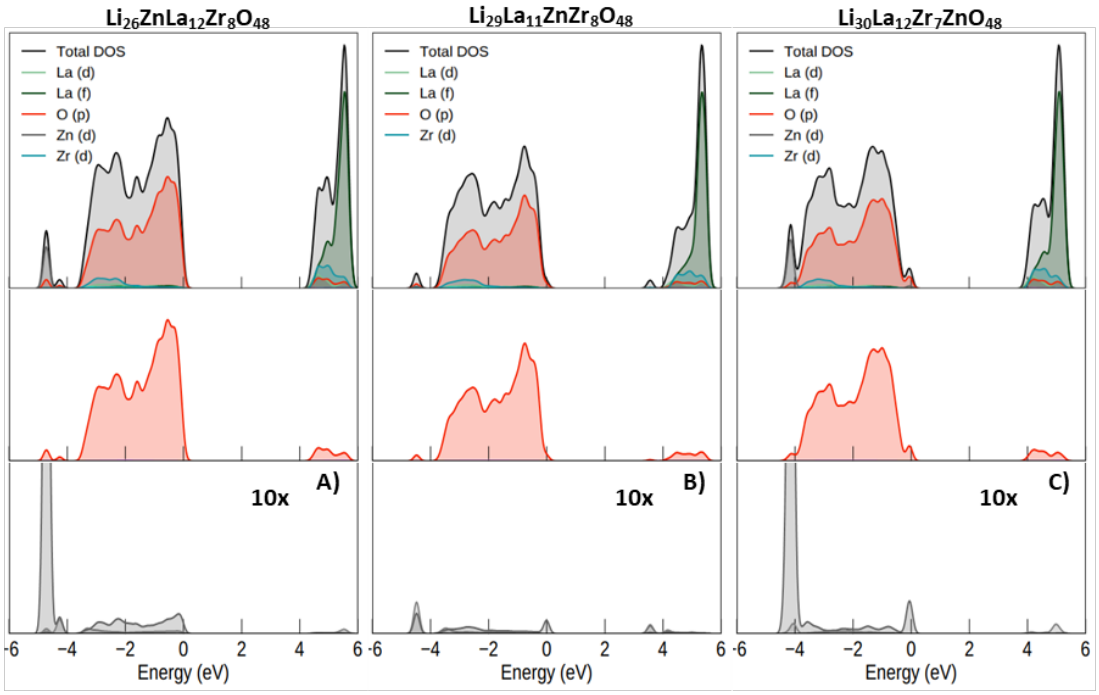

Figure 22: *The Density of States separated by atom for the Zn-doped LLZO at the Li2, Las3, and Zr5 sites*

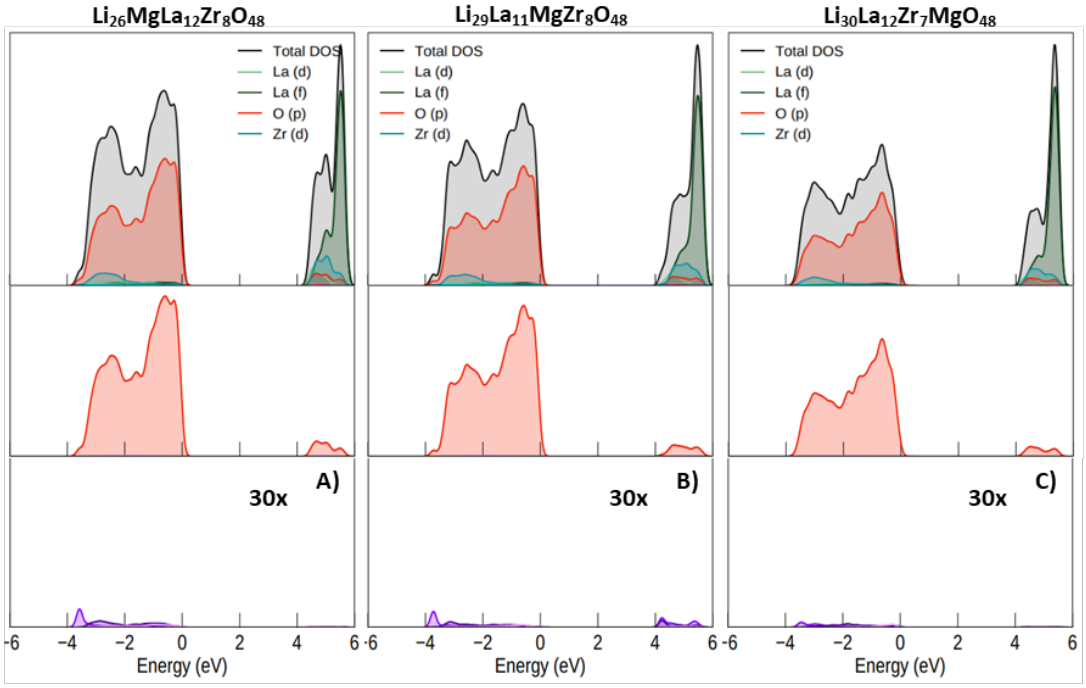

Figure 23: *The Density of States separated by atom for the Mg-doped LLZO at the Li2, Las3, and Zr5 sites*

5.4 Nudged Elastic Band Calculations

The experimental migration energy barrier for stoichiometric cubic LLZO is between 0.30-0.34 eV[12]. At the time of writing, no successful NEB jobs have been completed within a desirable range of accuracy or consistency in the calculations. The original outline to determine the lithium migration barriers included six hops (displayed in Figure 9) with 5-7 images each over nine dopant structures and and an additional three equivalent hops in the undoped LLZO structure. This required a total of 57 NEB calculations. Due to the expense of such a series of tests, this was eventually pared down to only 21 calculations for substitution at the lithium sites. The selected migration pathways were all found follow the same pattern of Li vacancy formation seen in Figure 24 when undergoing single hop migration. Due to the difficult nature of finding proper NEB parameters, extended waiting times for use of the systems, and lack of resources, the calculations had to be abandoned. This was a result of the size of the number of atoms within the system, adding to the complexity and the cost of calculating a single ionic hop.

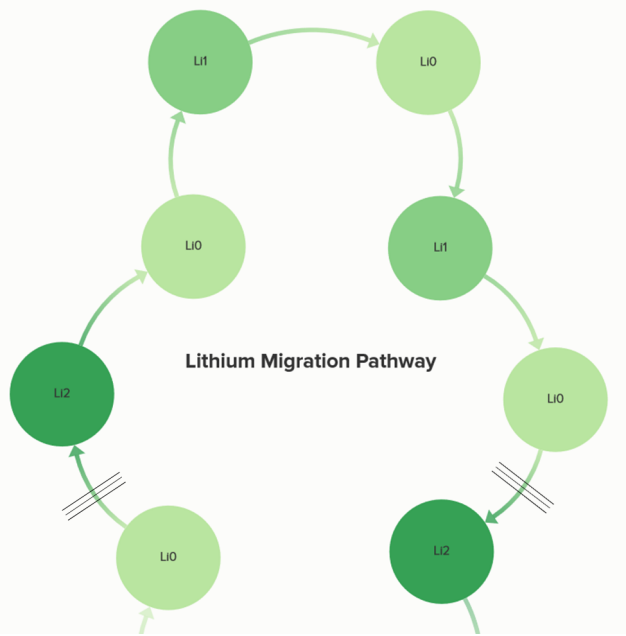

Figure 24: *Vacancy formation pattern in lithium migration pathways*

6 Discussion

6.1 Formation Enthalpy

The formation enthalpy is the benchmark calculation for the total energetic change that occurs during the ionic relaxation process in the defect structure. The formation enthalpy for each species is lowest, as expected, for the Li site substitution. Surprisingly, Mg demonstrates the lowest formation enthalpy. It was originally predicted that Zn would produce a lower value than both Al and Mg based on one significant study. They demonstrated a higher degree of Li site preference and thermodynamic stability for Zn than Al and Mg, which was shown to prefer the Zr-site[23]. All three dopants were tested at multiple sites with reported E_f values at the Li site of 1.32 eV (Zn), 1.36 eV (Al), and 1.63 eV (Mg). At the La site, they report 2.78 eV (Zn), 4.05 eV (Al), 2.38 eV (Mg) and at the Zr site they report 1.65 eV (Zn), 1.87 eV (Al), and 1.22 eV (Mg). The values compiled in Table A1 do not reflect those calculated in the referenced study, the reason for which is unknown. They adopt an energy cutoff of 500 eV and calculate their chemical potentials from the slope along a multiphase diagram from the structure composition towards the target element using the Pygmatgen analysis tools. The method for generating chemical potentials used in the current study is not relative to the phase composition of the doped LLZO system. To ensure that this was not the cause of the error, the same software was implemented to acquire chemical potential values for the defect structures in this study[68]. While the chemical potential dominates the formation enthalpy results in 4.1, the calculated values, of which there were several sets depending on the decomposition profile, were quite similar to those presented in 5.1. The PBEsol GGA functional is the same and PPs utilize the PAW method, so it is unlikely these parameters will differ greatly. Their internal database is used for generation of ionic substituted structures, which may produce some changes in the ionic positions. In the current study, Zn has the highest formation enthalpy across all V_{Li} distributions. As such, it is difficult to determine the cause of any discrepancies without comparing input files.

As it stands, the formation enthalpy does not seem to be indicative of physical or even relative results, so the results from this study are in question. Generally, the results are inconclusive and largely fail to reach agreement with previous computational or experimental work. However, within the following sections, a lengthy discussion on the data still provides some insights to the structural displacement and energetic changes within similar stoichiometric structures.

6.2 Relating Displacement and Formation Energy

As can be seen in Table A2 and the data presented in section5.2.1, there is clearly some relation between displacement and the formation energy. Initially, it was thought that Lanthanum and Zirconium site displacement would be the primary culprit behind high formation energy due to their higher chemical potentials presented in Table 2. The higher energy associated with these atoms means that movement across the lattice should theoretically result in a higher energy change

for the relaxed cell relative to a similar displacement by oxygen or lithium. The negatively charged vacancies that are not influenced by the positively charged dopant site due to distance or other positively charged atoms in the lattice will likely stabilize by displacing other nearby atoms.

It may be that since Zr^{4+} has a higher charge and associated energy, vacancy sites with fewer oxygen atoms, such as the highly stable Li2 sites, will have a greater binding effect on the Zr5 sites. Li2 sites are equally spaced between four Zr and three La sites. Li0 and Li1 are octahedral sites with close proximity to only two Zr and three La sites. The difference between these two sites is likely in the positioning of the La and Zr sites, which are somewhat linear and opposed relative to the Li1 site, whereas they are staggered relative to the Li0 site. The staggered formation allows for a greater degree of freedom than in the opposed forces seen at the Li1 site, which likely increases the overall displacement of these atoms surrounding the Li0 vacancies. So what accounts for the lower displacement in the Li2(i) position relative to the Li2(ii) position? While Li2(i) and Li2(ii) are of equal distance to the doping site at Li2(iii), the Li2(i) position is only partially obscured from the dopant site by either two Li0 sites or a single La4 site. The Li2(ii) position is obscured by a Zr5 site in any given direction, which may cause a greater displacement in the higher charged particles, accounting for the higher energy. The Li2(iv) position, which has a lower vacancy formation energy, is similarly obscured by Zr sites. However, it is in closer proximity to the Li2(iii) substitution site, it may have a minimal interaction with the charge imbalance. These may not be incredibly significant differences in conformation, but in such a small representation of the system with miniscule differences in energy between them, it may be that these slight differences account for the variations in formation energy. In the following paragraphs it is shown how these initial assumptions regarding La and Zr displacement are most likely overestimated but the positioning of the lithium sites may still hold some merit in elucidating the structural changes within the system.

Given the magnitude of displacement for each lithium position, formulated as f_{atom} in Section5.2.1, these initial observations don't quite hold up to closer scrutiny. Figure 14 and Figure 15 demonstrate these relationships for each $Zn_{Li2}\_V_{Li}$ structure. The magnitude of La and Zr displacement relative to the V_{Li1} and V_{Li0} sites is actually greater than that of the Li2 site. In the Li2 positions, Li2(i) is the only structure with a significant contribution from the La displacement and has a higher Zr displacement than its counterparts. Interestingly, the displacement of lithium and oxygen atoms constitutes a much more significant portion of the displacement. In the V_{Li2} sites, lithium displacement appears to constitute the bulk of the displacement involved in the higher formation energy. From Figure 14, Figure 15, Figure 17, and Figure 18, it can clearly be seen that Li0 atoms are the most prone to large displacements across all structures, which may be a result of their location relative to the La and Zr sites. There are sixteen Li0 sites, eight Li1 sites, and three Li2 sites that can be manipulated, so it might be expected that Li0 would have a higher magnitude. In breaking down the magnitude factor for each Li site, Li0 is less affected per atom than Li1 sites except for the highest

energy structures. Creating a vacancy at a Li2 site causes the greatest amount of displacement in Li0 sites, which is reflected in the inflated displacement factors for Li0 in these structures. Contrary to the initial observation, a higher magnitude of La or Zr displacement actually conserves energy in the system by limiting lithium displacement.

Similar to the vacancy structures discussed here, a systematic study of the displacement and formation energy at each interstitial position was presented in Figure 17, Figure 18, and Table A6. There are some obvious differences in the addition of a lithium interstitial that change the discussion relative to these structures. The displacement magnitude of the interstitial atom is much higher per atom than the other sites, even surpassing Li0 in the lowest energy structures. The interstitial needs to minimize its energy in the structure since it is placed in a geometrically determined position, requiring the formation of bonds with nearby anions in order to stabilize itself. The total vector displacement does not seem to trend higher or lower in magnitude relative to the formation energy, with some of the higher energy structures having the lowest displacement values. Through some observation, it can be noted that the more stable interstitial sites are positioned more evenly between high valence particles of Zn and La while high energy interstitial sites are positioned too close to one of these atoms or near several other lithium. However, there is not enough evidence to support this claim beyond speculation. There in no discernible trend in the data that explains the increase in formation energy apart from distance from the doping site. Even this measure fluctuates to a significant degree and cannot be relied on as a set rule.

Following these observations, it can be stated as a general rule that a vacancy at a Li0 or Li1 octahedral site will cause the least amount of disturbance in the system, leading to a lower formation energy than a V_{Li2} by 100-150meV. The interstitial sites give no conclusive trends apart from some minor correlations with dopant distance. The structural and displacement data alone is still inconclusive in fully determining the underlying causes of all changes in the formation energy. However, there is certainly a direct relation between the displacement, distance, and the resulting formation energy.

6.3 Defect Charge States

When a defect is introduced to the lattice in the form of a vacancy, interstitial or aliovalent dopant, there will be excess or a deficiency of electrons in the surrounding lattice where these defects occur. Some metal oxide materials undergo an oxidation or reduction of one of the adjacent cations to accommodate these electrons. This is also typically associated with an unwanted increase in electronic conductivity. However, between LLZO and the three dopants chosen, there are no cations that are susceptible to these effects under normal conditions. As such, excess electrons from the donor defects (think Al^{3+} at the Li^{+} site) would be expected to become 'trapped' at nearby oxygen sites, known as deep defect centers. Conversely, lithium vacancies act as acceptor defects and trap unpaired electrons from the nearby oxygens, which act as holes in the lattice for potential interstitial occupancies

and p-type conductivity. These impurities can be associated with either p- or n-type conductivity depending on the conditions, but both negatively impact ionic conductivity as they increase the interfering electronic conductivity in the system.

Normally, these defect centers exist in the band gap of the DOS diagram, extending the Fermi level beyond the top of the valence band. P-type acceptor defects lie closer to the valence band while n-type defects lie closer to the conduction band. Shallow traps lie close to the band edges and are associated with dopants that are similar in charge (+1 or -1) and atomic radius, such as Mg or Zn to the Li site. Deep traps are closer to the center of the band gap, and are associated with higher valency dopants or the additional perturbation of a nearby vacancy or interstitial. However, these traps can sometimes be resonant in the conduction or valence band and are thus not visible in the forbidden region (band gap). As can be seen in the results in Sections 5.3 and **??**, none of the resulting figures display a trap within the band gap. It could be due to the V_{Li} and Li_i sites, which are all in close proximity to the substitution sites for the calculated DOS structures. This could result in defect states that only appear resonantly deep within the opposing bands. The absence of oxygen defect states in the band gap points to favorable conductivity properties. The perturbations may have interacted with the excess electrons of the dopant cation as a result of being within 1-2 interatomic distances, a further clarification to the argument made in 6.2. An interatomic distance is defined here as 2.56 Å, the space between two Li atoms in the LLZO lattice following ion relaxation.

While it is likely that many have performed DOS calculations on defect structures for LLZO, only one data set was of DOS figures was found at the time of writing, which was for a series of oxygen vacancy charge states, where the traps were clearly visible in the band gap[34]. However, those defect states were directly linked to the trapping of the electron pair at the oxygen vacancy based on the resulting oxidation state. There were no defect states as a result of the doping material, which may confirm that there is no appreciable effect on the electronic conductivity as a result of doping at low concentrations. This further points to the beneficial properties of these dopant materials.

6.4 Site Preference

The structure as a whole is greatly affected at the site of the dopant substitution. A combination of charge valency, formation energies, and electronegativity considerations may elucidate the differences between dopants, their site preference, and the stability of the dopant in the target site. Table 1 Shows the relative charge and electronegativity for each ionic species in the current study. A in-depth study has shown the order of site preference for Al substitution in cubic LLZO to be Li (24d tetrahedral) > Li (96h octahedral) > Zr (16c) » La (24c)[86]. A similar trend would be expected for Zn, while Mg would be expected to have Zr site preference, with the other site preferences being unknown

Table 3 highlights the effects of each dopant on the selected site when comparing the displacement index (Z_{eff}) of the different doping sites with each of

the three dopants. The three dopants are conveniently varied in electronegativity and valence charge. Al_3^+ can be easily compared against Zn_2^+ with their similar electronegativity values, but different charges and ionic radii. Similarly, Mg can be compared against Zn for their difference in electronegativity while most other properties remain the same. As would be be expected, the higher charge and electronegativity of Al_3^+ resulted in tighter oxygen bonding in every single site following relaxation. It might also be predicted that Zn_2^+ would form tighter oxygen bonds than Mg_2^+, but this behaviour is only observed at the Li0 site. As discussed previously, the Li0 site is not as well guarded by neighboring high energy La and Zr atoms, lending more freedom of movement. In this instance, the six octahedrally bonded oxygen atoms are more exposed to covalent bonding forces from the multivalent dopants, resulting in a larger contraction for the zinc dopant. However, in the following sites, it is unclear why zinc binds less strongly than magnesium.

Are tight oxygen bonds a positive attribute? Do smaller interatomic forces localize the electron density, blocking lithium migration pathways? Or does this create a smaller steric effect, opening space in the lattice for more potential lithium vacancy sites and creating the disorder needed in the crystal lattice for stabilization of the cubic phase? Unfortunately, many of these questions are not able to be fully answered without further electrochemical and thermodynamic approximations. The discussion in the following sections (or previous???) will address how the lithium migration might be affected differently by the three dopants and may provide more insight to these questions.

The density of states data in Table 4 provides a relative sense of the electronic band gap, showing the favorable insulating properties that are desirable in an electrolyte material. These calculations have shown agreement with other calculated values using the PBEsol functional[35], but they are not accurate to physical conditions. As such, these values can only be compared internally. Of particular note is the greatly reduced band gap in the Al-doped Li0 site considering that the Zn- and Mg-doped structures demonstrated an improvement. This is in line with previous findings that aluminum may favor the Zr site. However, Al also has an extremely low formation energy at the Li site, so this small band gap may be indicative of other changes in the system. While the La-site does present favorably in this study, it creates no charge imbalance, thus no change in the lithium content. The creation of a vacancy or charge imbalance forces some change in the system, a key factor in the premise of the supervalent doping mechanism.

Zinc seems to show quite favorably in the Li position, performing well alongside the other two dopants in terms of formation energy and band gap. However, given the greatly decreased band gap for the La and Zr positions alongside formation energies that were consistently higher than magnesium, it is unlikely that zinc would perform as well as its divalent or trivalent counterparts. The lowest occupied orbitals that are responsible for decreasing the band gap in Zn are the La and Zr d-orbitals, which seem to be in line with the Zn orbitals. There is additionally a splitting of the Zn d-orbitals that occurs in the Zn_{Li2} structure. The splitting is accompanied by a generally increased contribution from the Zn-orbitals.

Magnesium, on the other hand, delivers the highest band gap for each configuration, showing a general stability in all three sites. Energetically, it may be that Mg favors the Li2 doping site, but may also experience doping at the La and Zr sites within the same sample, which would still be potentially beneficial in balancing the lithium content while still opening the structure to more lithium vacancy sites.

Based on the data gathered in this study, a general sense of the site preference for each dopant species can be assessed by examining the formation energy, site distortion, structural displacement, and density of states. A full determination of site preference could also potentially utilize some form of predictive MD method that could sample over all sites simultaneously. The feasibility of such a method has not been confirmed to the best knowledge of the researcher, but is simply proposed as an extension of the current study. Most existing methods utilized a similar method as the current study, although some have combined this with thermodynamic stability calculations, such as calculating the configurational entropy and experimental techniques like Rietveld refinement[87]. It has become more common to calculate the formation entropy alongside the formation enthalpy and free energy in describing point defects in ionic solids, due to the creation of lithium vacancies that are accompanied by lithium delocalization and disordering. The configurational entropy and other thermodynamic properties are essential to calculate the temperature dependence of the concentration of point defects from the formation free energy[88]. It can be assumed that a highly entropic defect formation would favor the cubic phase at lower temperatures. However, there are several setbacks to calculating the formation entropy that have limited its use to only specific applications. Primarily, it is not yet well defined, particularly in relation to the role that phonons take on in the formalized definition of entropy. The methods for calculating the phonon vibrational spectrum is ill-defined and computationally expensive or results in large numerical errors and finite, size-dependents results. The calculations lay outside the scope of the current study and were thus not taken into account. Additionally, the free enthalpy is synonymous with the defect energy of formation and largely dominates the free energy term.

To conclude, the compiled data does give some indication to the site preference of each dopant species based on formation energies, distortion, and overall displacement. $Al_3{}^+$ shows an affinity to the $Zr_4{}^+$ site, matched by a low formation energy and large band gap. Zn clearly favors the tetrahedral Li2 site, although it may also be possible that substitution occurs at the La site. A high formation energy and small band gap indicate that the Zn'''_{Zr} substitution may have a prohibitively high defect energy. Mg has showed the most consistent data with relatively low formation energies and large band gaps for each dopant site. This indicates that there is little strong preference made for substitution at any given site, leading the final doped compound to contain partial occupancies of the $Mg_2{}^+$ species at several site throughout the lattice. This could result in a high amount of lattice disorder that may result in highly favorable properties such as those described previously for the Mg-doped system.

One key quality lacking in this study was the consideration of more defect

compositions, such as $V_O^{\bullet\bullet}$ or cation antisites. These may have provided a more clear picture of the potential substitution mechanisms in each of the target dopant species, particularly the La and Zr substitutions, where the additional of an interstitial appears to have been energetically unfavorable. Additionally, it should be considered whether low energy interstitials can form at 16e vacancies by redistribution of high energy occupied Li sites. This could be determined by and electrostatic energy criterion such as Ewald's summation[23].

6.5 The Cubic Phase

As stated previously, the cubic phase of LLZO is formed during high temperature sintering. The tetragonal phase transition occurs during the cooling process. The cubic phase can be stabilized at lower temperatures through the addition of dopant metals with a difference in valence, such as those presented in the current study. The primary mechanism through which this occurs is in the creation of lithium vacancy sites that create disorder in the lithium sublattice and reduce lithium content. A redistribution of the vacancy sites occurs during the phase transitions, with the doped structures having a greatly disorded lithium sublattice, resulting in a reduced free energy that promotes the cubic phase. The full occupancy and ordering of the tetragonal phase does not exist in the cubic phase, even though the two phases are quite similar in structure and form. The latter forms partial lithium occupancies governed by inherent energetics limiting site occupancy[25]. Some studies have found that these vacancies tend to distribute at active octahedral sites, not those most influenced by the doped atom. This is most likely a result of the blocking effect that these dopants may have on the lithium migration pathways. Vacancies will naturally redistribute to a lower energy conformation that would occur during lithium migration.

Modelling the structural phase transition is extremely complex and not well understood. Previous studies have used a combination of DFT relaxations of the initial and final structures coupled with MD calculations between the two structures in order to better elucidate the time-dependent structural changes that take place within the phase transition[15, 14]. This is generally computationally heavy and time-consuming, so this was not imitated in the current study. The data within this study is insufficient to properly indicate the effectiveness of each dopant to enact the cubic phase stabilization, but through the distortion at the dopant site and Li^+ delocalization, some clues can be obtained. Ideally, a second set of cubic phase structures would have been generated with the doped sites. However, this introduces several issues with site redistribution. Since the cubic phase has more potential Li sites, a large number of structures would need to be generated to reflect the random distribution of Li ions and their respective energies. Further, the lattice parameters between the two structures would invariably change, so it would be difficult to compare the two phases accurately. Due to these factors and time constraints, it was deemed unnecessary to pursue these additional investigations under the current study.

Localized distortion of the oxygen bonds at the site of dopant substitution

accounts for a significant change in the sublattice structure. $Al_3{}^+$ substitution, which is known to stabilize the cubic phase, results in the greatest contractions in the O-bonds in Table 3, but it can also be seen that this occurs in the less stable or unfavorable doping sites. Substitution at the Li2 and Zn5 sites, which have been argued in Section6.4 to be the preferred sites for $Al_3{}^+$, results in a smaller deviation. This seems to indicate that finding a dopant capable of stabilizing the doping site while still increasing the disorder in the lithium sublattice could be an important factor to consider when screening for new dopants in future studies.

Any further analysis of the data is purely conjecture. Without sampling across the transition states, there is not much that can be said about the efficacy of the Zn and Mg dopants in stabilizing the cubic phase beyond the comparisons to the reference dopant Al that have been provided within this study. Both dopants appear to have similar or improved properties to the the reference, so it is likely that they would also achieve this phase transition successfully.

6.6 Lithium Migration

Figure 24 highlights another consideration in vacancy site formation. Li2 sites are limited in quantity and a necessary hopping site along all observable lithium migration pathways. As previously mentioned, other studies have theorized that aluminum doping at the Li2 site traps or hinders migrating Li^+ ions[37]. This is due to the looped structure of Li lattice formation introduced by Awaka et. al[13]. Here, the Li sites form a ring around either a Zr5 or La4 site with the following pattern: -Li2-Li0-Li1-Li0-Li2-Li0-Li1-Li0-. Li2 connects these ring structures as the intersection point, serving an important structural role and lying directly along the migration pathways. The loop structure is visualized in Figure 25 This is further proof for the stability of Li2 sites and the high formation energy of vacancies at these sites. Additionally, if substitution at these sites does block Li-migration, then doping at either the Zr or La site may encourage Li migration to a greater degree. An important question that may arise from this conclusion is if it is possible to engineer the substitution mechanism to ensure favorable site selection. A previous work[34] has investigated the defect energy and concentration of various defects under different chemical potential conditions: oxygen poor/rich, Li metal poor/rich, etc. This same methodology combined with careful control of temperature, pressure, and synthesis method could ensure more direct doping mechanisms. Some amount of disorder is beneficial to the material, strengthening mechanical properties, preventing dendrite growth, stabilizing desirable phases, and lowering electronic conductivity.

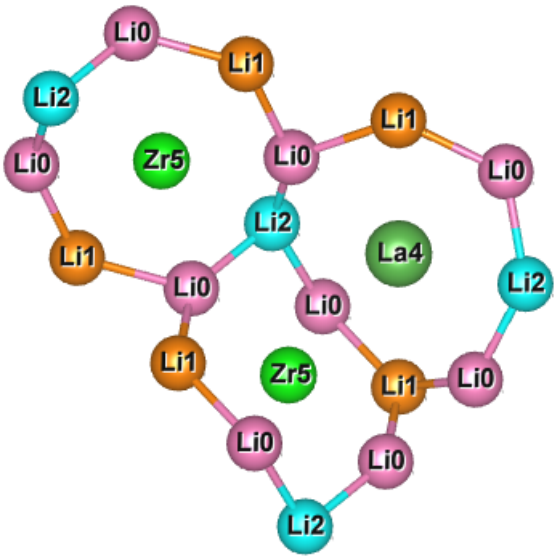

Figure 25: *A section of the LLZO unit cell highlighing the Looped Li-site structure composing the Li sub-lattice, proposed by Awaka et. al.[13]*

Vacancies in the active octahedral sites are key to fast ionic conductivity[26, 37], since these sites form along active lithium migration pathways as opposed to channels that are suppressed or blocked by the aliovalent dopant. There were several possible three-dimensional migration pathways that intersect and allow varied migration patterns for the Lithium ions, but only a few pathways were selected due to the large number of structures that are involved in such calculations. Previous studies have already addressed the lithium migration barriers in the tetragonal LLZO structure. While 3D migration is geometrically possible, Chen et. al[15] reported that only transport in the *ab* plane is energetically possible below a temperature threshold, 900K. The difference between the cubic and tetragonal phase lies only in the Li-Li pair distance and redistribution of Li more evenly along two inequivalent sites, as opposed to four in the tetragonal phase, only three of which can be occupied under normal conditions. They further suggest that 16f (Li1) sites are responsible for hindering transport in the c direction, instead proposing an unoccupied tetrahedral 16e site for lithium migration that would fit between the Li1 and Li0 sites in Figure 25[13, 15]. The 16e site was mistakenly overlooked in the current study, with all migration paths passing through the 16f site. If their findings are correct, this may account for some of the difficulties experienced in convergence of the NEB calculations.

Furthermore, concerted migration is predicted to be favored in Tetragonal LLZO vs the single-ion hopping in the cubic structure. Concerted migration is far more complex to calculate and the methods that have been previously established cannot possibly account for the complexity of coordinated forces and simultaneous sampling of dozens of potential migration pathways for each transported ion. AIMD has been suggested as a potential method, but is computationally heavy and can only sample over a select portion of the bulk material[29, 26]. This fails

to account for potential surface and bulk lattice effects. Calculation of the migration barriers in the cubic structure is not well understood by DFT either, since there is a constant partial occupancy and disorder in the Li sub-lattice that allows for shifting of Li atoms to accommodate Li migration[26]. This is also difficult to accurately model given current advancements in the computing field, but still less complex than concerted migration. However, both methods yield good approximations that better elucidate the structural changes that occur at an atomic level. For reasons stated previously, the cubic phase offered other challenges for the current study (see Section 6.5), so lithium migration was not attempted for the cubic phase. Future studies could potentially build off of the framework established within to establish the cubic phase and conduct NEB calculations within this framework instead. Alternatively, development of the single-ion hop along the 16e vacancies may allow for more easily converged calculations that can yield the comparative results desired within the current study.

7 Conclusion

7.1 A Final Analysis of Dopant Suitability

Through a systematic study of site preference and vacancy/interstitial formation, the cations Al, Zn, and Mg were tested as dopants in the solid state electrolyte material, LLZO. With favorable formation enthalpies and similar properties to the Al dopant, it would seem that Mg and Zn are both viable dopants. However, the data here is insufficient to fully describe the cubic phase transition, which is the primary purpose in doping the LLZO system, although the data does provide some hints as to whether this transition will be favorable. This is mainly seen through the disordering of the lithium sub-lattice, which can bee seen in the high lithium displacement values seen in Section 5.2.1. Additionally, the relative stability of the dopants at the Li2 site implies a limited interaction with the nearby active sites in the lithium migration pathway. A continuation of this work would preferably continue with modeling the phase transition and defining migration energy barriers and active migration pathways for each dopant. Additionally, the initial predicted site preference is only loosely supported by the data. The formation enthalpy for Mg and Al substitution at the Zr site were well out of the expected trend based on previous studies and initial expectations based on ionic characteristics. If there was a miscalculation of the formation enthalpies, the error was not determined at the time of writing, although it may be linked to the overly simplified direct-charge compensation model assumed in the study.

7.2 Future Work

While the current study may be useful in analyzing the base energies associated with supervalent doping, it may not fully account for the effect of the phase transition that occurs as a result. Concerted migration may serve as the primary mechanism in the tetragonal phase lithium ion migration[26], while the single-ion

hopping mechanism has been shown to have a greater contribution in the cubic phase[25]. Thus, further work would examine the transition state energies of each dopant in the tetragonal phase by means of concerted miration. Additionally, by utilizing the methodological framework established in Meier et. al.[25] and the structural data from Awaka et. al.[13], it is possible to build a representative profile of the random distribution of lithium ions in all available vacancy sites in the cubic phase. This would allow for a more thorough investigation of the migratory pathways that arise as a result of the disordering caused by introduction of the dopant species into the LLZO crystal lattice. A combination of molecular dynamics and DFT could be vital in examining the favorable structural properties associated with the Zinc and Magnesium dopants in stabilizing the cubic phase, preventing tetragonal phase transition.

LLZO is vulnerable to degradation at the grain boundary and surface layer in contact with atmospheric conditions, particularly moisture and CO_2 into its non-conducting substituent compounds, La_2O_3, Li_2CO_3, and LiOH. This increases the interfacial resistance at both the cathode and anode, reducing total conductivity. It can also create "pockets" of lithium ion buildup as the lattice degrades over time, reducing the energy capacity of the cell[11]. Magnesium may prevent decay of LLZO at the interface into subsidiary compounds[39]. If so, Zinc may prove to have similar properties due to its similar ionic radius, valence charge, and thermodynamic stability[23]. Interfacial density of states calculations can infer the stability of the desired phase at these critical junctions. Further continuation of this project can use computational methods to study the mechanisms of surface compound formation and the validity of claims regarding Mg's ability to dampen this effect. Should this prove successful, Zn may also be investigated to reveal if it possesses similar properties.

The current study did not account for more complex native point defects, such as oxygen vacancies and other cationic species that form antisites under varying synthesis conditions. These formation properties may more accurately represent the lithium composition present upon aliovalent doping[34]. A systematic introduction of more complex defect formation may reveal a more favorable site preference for each of the dopant species, providing a more well-rounded understanding of the dopants in this study as well as building a framework for any number of dopant species that may have desirable properties.

The scale of complexity, time, and resources renders these methods out of the scope of the current study and were thus excluded. Future studies may build off the framework established herein, perhaps exploring some of these methods in more detail.

References

[1] "Statistics Time Series". In: *IRENA: International Renewable Energy Agency* (2020).

[2] Rui Sousa et al. "All-solid-state batteries: An overview for bio applications". In: Feb. 2013.

[3] "The Nobel Prize in Chemistry 2019". In: *NobelPrize.org* ().

[4] "Announcement of New Lithium Ion Batteries, Realizing Industry's Highest Level of Energy Density". In: *Sony Global* (Dec. 2004).

[5] Sampathkumar Ramakumar et al. "Lithium garnets: Synthesis, structure, Li+ conductivity, Li+ dynamics and applications". In: *Progress in Materials Science* 88 (Apr. 2017).

[6] Candace K. Chan, Ting Yang, and J. Mark Weller. "Nanostructured Garnet-type Li7La3Zr2O12: Synthesis, Properties, and Opportunities as Electrolytes for Li-ion Batteries". In: *Electrochimica Acta* 253 (2017), pp. 268–280. ISSN: 0013-4686.

[7] John B. Goodenough and Youngsik Kim. "Challenges for Rechargeable Li Batteries". In: *Chemistry of Materials* 22.3 (2010), pp. 587–603.

[8] Noriaki Kamaya et al. "A lithium superionic conductor". In: *Nature Materials* 10 (Sept. 2011), pp. 682–686.

[9] Wei Luo et al. "Reducing Interfacial Resistance between Garnet-Structured Solid-State Electrolyte and Li-Metal Anode by a Germanium Layer". In: *Advanced Materials* 29.22 (2017), p. 1606042.

[10] Xin-Bing Cheng et al. "Toward Safe Lithium Metal Anode in Rechargeable Batteries: A Review". In: *Chemical Reviews* 117.15 (2017). PMID: 28753298, pp. 10403–10473. eprint: https://doi.org/10.1021/acs.chemrev.7b00115.

[11] Hong-Kang Tian, Bo Xu, and Yue Qi. "Computational study of lithium nucleation tendency in Li7La3Zr2O12 (LLZO) and rational design of interlayer materials to prevent lithium dendrites". In: *Journal of Power Sources* 392 (2018), pp. 79–86. ISSN: 0378-7753.

[12] Ramaswamy Murugan, Venkataraman Thangadurai, and Werner Weppner. "Fast Lithium Ion Conduction in Garnet-Type Li7La3Zr2O12". In: *Angewandte Chemie International Edition* 46.41 (2007), pp. 7778–7781. eprint: https://onlinelibrary.wiley.com/doi/pdf/10.1002/anie.200701144.

[13] J. Awaka et al. "Synthesis and structure analysis of tetragonal Li7 La3 Zr2 O12 with the garnet-related type structure". In: *Journal of Solid State Chemistry* 182 (2009), pp. 2046–2052.

[14] N. Bernstein, M. D. Johannes, and Khang Hoang. "Origin of the Structural Phase Transition in $Li_7La_3Zr_2O_{12}$". In: *Phys. Rev. Lett.* 109 (20 Jan. 2012), p. 205702.

[15] Fei Chen et al. “Origin of the Phase Transition in Lithium Garnets”. In: *The Journal of Physical Chemistry C* 122.4 (2018), pp. 1963–1972. eprint: https://doi.org/10.1021/acs.jpcc.7b10911.

[16] Charles A. Geiger et al. “Crystal Chemistry and Stability of “Li7La3Zr2O12” Garnet: A Fast Lithium-Ion Conductor”. In: *Inorganic Chemistry* 50.3 (2011), pp. 1089–1097.

[17] Ezhiyl Rangasamy, Jeff Wolfenstine, and Jeffrey Sakamoto. “The role of Al and Li concentration on the formation of cubic garnet solid electrolyte of nominal composition Li7La3Zr2O12”. In: *Solid State Ionics* 206 (2012), pp. 28–32. ISSN: 0167-2738.

[18] Travis Thompson et al. “Tetragonal vs. cubic phase stability in Al – free Ta doped Li7La3Zr2O12 (LLZO)”. In: *J. Mater. Chem. A* 2 (33 2014), pp. 13431–13436.

[19] Rajendra [Hongahally Basappa] et al. “Grain boundary modification to suppress lithium penetration through garnet-type solid electrolyte”. In: *Journal of Power Sources* 363 (2017), pp. 145–152. ISSN: 0378-7753.

[20] Alfred Junio Samson et al. “A bird’s-eye view of Li-stuffed garnet-type Li7La3Zr2O12 ceramic electrolytes for advanced all-solid-state Li batteries”. In: *Energy Environ. Sci.* 12 (10 2019), pp. 2957–2975.

[21] Lei Cheng et al. “Effect of Surface Microstructure on Electrochemical Performance of Garnet Solid Electrolytes”. In: *ACS Applied Materials & Interfaces* 7.3 (2015). PMID: 25563572, pp. 2073–2081. eprint: https://doi.org/10.1021/am508111r.

[22] Yosuke Suzuki et al. “Transparent cubic garnet-type solid electrolyte of Al2O3-doped Li7La3Zr2O12”. English. In: *Solid State Ionics* 278 (June 2015), pp. 172–176. ISSN: 0167-2738.

[23] Lincoln J. Miara et al. “First-Principles Studies on Cation Dopants and Electrolyte|Cathode Interphases for Lithium Garnets”. In: *Chemistry of Materials* 27.11 (2015), pp. 4040–4047.

[24] Anubhav Jain et al. “Commentary: The Materials Project: A materials genome approach to accelerating materials innovation”. In: *APL Materials* 1.1 (2013), p. 011002. ISSN: 2166532X.

[25] Katharina Meier, Teodoro Laino, and Alessandro Curioni. “Solid-State Electrolytes: Revealing the Mechanisms of Li-Ion Conduction in Tetragonal and Cubic LLZO by First-Principles Calculations”. In: *The Journal of Physical Chemistry C* 118.13 (2014), pp. 6668–6679. eprint: https://doi.org/10.1021/jp5002463.

[26] Xingfeng He, Yizhou Zhu, and Yifei Mo. “Origin of fast ion diffusion in super-ionic conductors”. In: *Nature Communications* 8.1 (2017).

[27] Henrik Buschmann et al. “Structure and dynamics of the fast lithium ion conductor “Li7La3Zr2O12””. In: *Phys. Chem. Chem. Phys.* 13 (43 2011), pp. 19378–19392.

[28] Chi Chen, Ziheng Lu, and Francesco Ciucci. "Data mining of molecular dynamics data reveals Li diffusion characteristics in garnet Li7La3Zr2O12". In: *Scientific Reports* 7.1 (2017).

[29] Randy Jalem et al. "Concerted Migration Mechanism in the Li Ion Dynamics of Garnet-Type Li7La3Zr2O12". In: *Chemistry of Materials* 25.3 (2013), pp. 425–430. eprint: https://doi.org/10.1021/cm303542x.

[30] L. Vegard. "Die Konstitution der Mischkristalle und die Raumfüllung der Atome". In: *Z. Physik* 5 (1921), pp. 17–26.

[31] A. R. Denton and N. W. Ashcroft. "Vegard's law". In: *Phys. Rev. A* 43 (6 Mar. 1991), pp. 3161–3164.

[32] Saikat Mukhopadhyay et al. "Structure and Stoichiometry in Supervalent Doped Li7La3Zr2O12". In: *Chemistry of Materials* 27.10 (2015), pp. 3658–3665.

[33] F. Kroger and H. Vink. "Relations between the concentrations of imperfections in crystalline solids". In: *Solid State Physics* 3 (1956), pp. 307–435.

[34] Alex Squires, David Scanlon, and Benjamin Morgan. "Native Defects and their Doping Response in the Lithium Solid Electrolyte Li7La3Zr2O12". In: (2019).

[35] Ashkan Moradabadi and Payam Kaghazchi. "Defect chemistry in cubic Li6.25Al0.25La3Zr2O12 solid electrolyte: A density functional theory study". In: *Solid State Ionics* 338 (2019), pp. 74–79. ISSN: 0167-2738.

[36] Stephen R. Yeandel et al. "Structure and Lithium-Ion Dynamics in Fluoride-Doped Cubic Li7La3Zr2O12 (LLZO) Garnet for Li Solid-State Battery Applications". In: *The Journal of Physical Chemistry C* 122.49 (2018), pp. 27811–27819. eprint: https://doi.org/10.1021/acs.jpcc.8b07704.

[37] Yan Chen et al. "Origin of High Li Conduction in Doped Li7La3Zr2O12 Garnets". In: *Chemistry of Materials* 27.16 (July 2015), pp. 5491–5494.

[38] X. Yang, D. Kong, and Z. Chen. "Low-temperature fabrication for transparency Mg doping Li7La3Zr2O12 solid state electrolyte". In: *J Mater Sci: Mater Electron* 29 (2018), pp. 1523–1529.

[39] Amardeep, Sushobhan Kobi, and Amartya Mukhopadhyay. "Mg-doping towards enhancing the composition-phase-structural stability of Li-La-zirconate based cubic garnet upon exposure to air". In: *Scripta Materialia* 162 (2019), pp. 214–218. ISSN: 1359-6462.

[40] J.L. Allen et al. "Effect of substitution (Ta, Al, Ga) on the conductivity of Li7La3Zr2O12". In: *Journal of Power Sources* 206 (2012), pp. 315–319. ISSN: 0378-7753.

[41] Reinhard Wagner et al. "Fast Li-Ion-Conducting Garnet-Related Li7–3xFexLa3Zr2O12 with Uncommon I43d Structure". In: *Chemistry of Materials* 28.16 (Oct. 2016), pp. 5943–5951.

[42] Venkataraman Thangadurai, Heiko Kaack, and Werner Weppner. "Novel fast lithium ion conduction in garnet-type Li5La3M2O12 (M = Nb, Ta)". In: *Journal of the American Ceramic Society* 86 (Mar. 2003), pp. 437–440.

[43] Ramaswamy Murugan, S. Ramakumar, and N. Janani. "High conductive yttrium doped Li7La3Zr2O12 cubic lithium garnet". In: *Electrochemistry Communications* 13.12 (2011), pp. 1373–1375. ISSN: 1388-2481.

[44] R. D. Shannon. "Revised effective ionic radii and systematic studies of interatomic distances in halides and chalcogenides". In: *Acta Crystallographica Section A* 32.5 (Sept. 1976), pp. 751–767.

[45] Yan Chen et al. "Origin of high Li+ conduction in doped Li7 La3 Zr2 O12 garnets". In: *Chemistry of Materials* 27 (2015), pp. 5491–5494.

[46] Don L. Anderson. *Theory of the Earth.* Boston, Ma: Blackwell Scientific Publications. ISBN: 0865423350.

[47] David Sholl, Janice A. Steckel, and Sholl. *Density Functional Theory: a Practical Introduction.* Wiley, 2011.

[48] J.G. Lee. *Computational Materials Science: An Introduction, Second Edition.* CRC Press, 2016. ISBN: 9781498749763.

[49] G. Kresse and J. Hafner. "Ab initio molecular dynamics for liquid metals". In: *Phys. Rev. B.* 47.558 (1993).

[50] G. Kresse and J. Hafner. "Ab initio molecular-dynamics simulation of the liquid-metal-amorphous-semiconductor transition in germanium". In: *Phys. Rev. B.* 49.14251 (1994).

[51] G. Kresse and J. Furthmüller. "Efficiency of ab-initio total energy calculations for metals and semiconductors using a plane-wave basis set". In: *Comput. Mat. Sci.* 6.15 (1996).

[52] G. Kresse and J. Furthmüller. "Efficient iterative schemes for ab initio total-energy calculations using a plane-wave basis set". In: *Phys. Rev. B,* 54.11169 (1996).

[53] M. Born and R. Oppenheimer. "On the Quantum Theory of Molecules." In: *Annalen der Physik* 389.20 (1927), pp. 457–484.

[54] Thomas Engel and Philip Reid. *Quantum chemistry & spectroscopy.* Pearson, 2013.

[55] P. Hohenberg and W. Kohn. "Inhomogeneous Electron Gas". In: *Phys. Rev.* 136 (3B Nov. 1964), B864–B871.

[56] W. Kohn and L. J. Sham. "Self-Consistent Equations Including Exchange and Correlation Effects". In: *Phys. Rev.* 140 (4A Nov. 1965), A1133–A1138.

[57] John P. Perdew et al. "Restoring the Density-Gradient Expansion for Exchange in Solids and Surfaces". In: *Phys. Rev. Lett.* 100 (13 Apr. 2008), p. 136406.

[58] H Hellmann. In: *Einfuhrung in die Quantumchemie* 54.11-12 (1937).

[59] R. P. Feynman. “Forces in Molecules”. In: *Physical Review* 56.4 (1939), pp. 340–343.

[60] Søren Smidstrup et al. “Improved initial guess for minimum energy path calculations”. In: *The Journal of Chemical Physics* 140.21 (2014), p. 214106. eprint: https://doi.org/10.1063/1.4878664.

[61] Graeme Henkelman, Blas P. Uberuaga, and Hannes Jónsson. “A climbing image nudged elastic band method for finding saddle points and minimum energy paths”. In: *The Journal of Chemical Physics* 113.22 (2000), pp. 9901–9904. eprint: https://doi.org/10.1063/1.1329672.

[62] Hendrik J. Monkhorst and James D. Pack. “Special points for Brillouin-zone integrations”. In: *Phys. Rev. B* 13 (12 June 1976), pp. 5188–5192.

[63] P.E Blochl. “Projector augmented-wave method”. In: *Phys. Reb. B.* 50.17953 (1994).

[64] G. Kresse and D. Joubert. “From ultrasoft pseudopotentials to the projector augmented-wave method”. In: *Phys. Rev. B.* 59.1758 (1999).

[65] G Kresse and J Hafner. “Norm-conserving and ultrasoft pseudopotentials for first-row and transition elements”. In: *Journal of Physics: Condensed Matter* 6.40 (Oct. 1994), pp. 8245–8257.

[66] David Vanderbilt. “Soft self-consistent pseudopotentials in a generalized eigenvalue formalism”. In: *Phys. Rev. B* 41 (11 Apr. 1990), pp. 7892–7895.

[67] Yu Kumagai and Fumiyasu Oba. “Electrostatics-based finite-size corrections for first-principles point defect calculations”. In: *Physical Review B* 89.19 (May 2014). ISSN: 1550-235X.

[68] Shyue Ping Ong et al. “Python Materials Genomics (pymatgen) : A Robust, Open-Source Python Library for Materials Analysis.” In: *Computational Materials Science* 68 (2013), pp. 314–319.

[69] Koichi Momma and Fujio Izumi. “*VESTA3* for three-dimensional visualization of crystal, volumetric and morphology data”. In: *Journal of Applied Crystallography* 44.6 (Dec. 2011), pp. 1272–1276.

[70] A. Logeat et al. “From order to disorder: the structure of lithium-conducting garnets Li7-x La3 Tax Zr2-x O12 (x = 0 - 2)”. In: *Solid State Ionics* 206 (2012), pp. 33–38.

[71] Yuxing Wang, Ashfia Huq, and Wei Lai. “Insight into lithium distribution in lithium-stuffed garnet oxides through neutron diffraction and atomistic simulation: Li7-x La3 Zr2-x Tax O12 (x = 0-2) series”. In: *Solid State Ionics* 255 (2014), pp. 39–49.

[72] K. Lejaeghere et al. “Error Estimates for Solid-State Density-Functional Theory Predictions: An Overview by Means of the Ground-State Elemental Crystals”. In: *Critical Reviews in Solid State and Materials Sciences* 39.1 (2014), pp. 1–24. eprint: https://doi.org/10.1080/10408436.2013.772503.

[73] C. Kittel. *Introduction to Solid State Physics*. Vol. 8. New York: Wiley, 1976, p. 139.

[74] L. J. Sham and M. Schlüter. "Density-Functional Theory of the Energy Gap". In: *Phys. Rev. Lett.* 51 (20 Nov. 1983), pp. 1888–1891.

[75] Travis Thompson et al. "Electrochemical Window of the Li-Ion Solid Electrolyte Li7La3Zr2O12". In: *ACS Energy Letters* 2.2 (2017), pp. 462–468.

[76] Henkelman group. *VTSTTools3.1*. University of Texas, Austin, TX, USA.

[77] Handan Yildirim et al. "Calculated Pre-exponential Factors and Energetics for Adatom Hopping on Terraces and Steps of Cu(100) and Cu(110)". In: *Surface Science* 600 (July 2005), pp. 484–492.

[78] George H. Vineyard. "Frequency factors and isotope effects in solid state rate processes". In: *Journal of Physics and Chemistry of Solids* 3.1 (1957), pp. 121–127. ISSN: 0022-3697.

[79] Ulrike Kürpick, Abdelkader Kara, and Talat. S. Rahman. "Role of Lattice Vibrations in Adatom Diffusion". In: *Phys. Rev. Lett.* 78 (6 Feb. 1997), pp. 1086–1089.

[80] U. Kurpick and T.S. Rahman. In: *Phys. Rev. B.* 57 (1998), p. 2482.

[81] U. Kurpick and T.S. Rahman. In: *Surf. Sci.* 15-21 (1999), pp. 427–428.

[82] U. Kurpick and T.S. Rahman. In: *Phys. Rev. B.* 59 (1999), p. 11014.

[83] Henry Eyring. "The Activated Complex in Chemical Reactions". In: *The Journal of Chemical Physics* 3.2 (1935), pp. 107–115.

[84] Kazutoshi Miwa and Ryoji Asahi. "Molecular dynamics simulations with machine learning potential for Nb-doped lithium garnet-type oxide $Li_{7-x}La_3(Zr_{2-x}Nb_x)O_{12}$". In: *Phys. Rev. Materials* 2 (10 Oct. 2018), p. 105404.

[85] Alex Ganose, Adam Jackson, and David Scanlon. "sumo: Command-line tools for plotting and analysis of periodic *ab initio* calculations". In: *Journal of Open Source Software* 3.28 (2018), p. 717.

[86] Daniel Rettenwander et al. "DFT Study of the Role of Al3+ in the Fast Ion-Conductor Li7–3xAl3+xLa3Zr2O12 Garnet". In: *Chemistry of Materials* 26.8 (2014), pp. 2617–2623.

[87] Jacek Zeglinski et al. "Unravelling the specific site preference in doping of calcium hydroxyapatite with strontium from ab initio investigations and Rietveld analyses". In: *Phys. Chem. Chem. Phys.* 14 (10 2012), pp. 3435–3443.

[88] Seeberger, Pia and Vidal, Julien. "On the ab initio calculation of vibrational formation entropy of point defect: the case of the silicon vacancy". In: *EPJ Photovolt.* 8 (2017), p. 85505.

[89] Z. Deng et al. "Data-Driven First-Principles Methods for the Study and Design of Alkali Superionic Conductors". In: *Chem. Mater.* (2016).

Appendix

A Resources

A.1 Pymatgen

Pymatgen (Python Materials Genomics) is an open-source Python library for materials analysis [89, 68]. It provides class objects for the Element, Site, Molecule, and Structure types. This serves as a great framework for phase, electronic, and structural analysis as well as more specialized features. In particular, the current study has extensively made use of the pymatgen diffusion module, which provides NEB migration pathways and IDPP image structures. It has also been manipulated quite a bit to produce more manual pathways and structural changes as best suited the direct needs of the project. In particular the code has been adapted to create a pathway between any two vacancies in the structure if the coordinates or sites are known. However, this is not recommended nor is it highly realistic of physical conditions unless the user takes great care. The script used for this has been provided the Supplementary information data package.

B Additional Data

B.1 Relaxation Energies

Table A1: *Final Representative Structures*

Structure	E_0	E_{diff}	E_f	E_f/**f.u.**
LLZO	-715.806	0.0000	N/A	N/A
$Al_{Li2}\_V_{Li0}\_V_{Li0}$	-712.879	2.927	5.395	1.349
$Mg_{Li2}\_V_{Li0}$	-712.697	3.109	5.356	1.339
$Zn_{Li2}\_V_{Li0}$	-710.329	5.476	5.804	1.451
Al_{La3}	-710.920	4.886	7.121	1.780
Mg_{La3}+Li_i(**0**)	-711.482	4.323	6.337	1.584
Zn_{La3}+Li_i(**0**)	-709.118	6.688	6.782	1.695
Al_{Zr5}+Li_i(**x**)	-711.088	4.717	7.683	1.921
Mg_{Zr5}+Li_i(**x**)+Li_i(**xv**)	-710.082	5.723	8.468	2.117
Zn_{Zr5}+Li_i(**x**)+Li_i(**xv**)	-707.149	8.657	9.482	2.370

Table A2: *Vacancy Energy to Distance and Displacement*

Structure	E_f	**Distance (Å)**	d_{sum}	d_{vector} **(Å)**
$Zn_{Li2}\_V_{Li0}$**(xvi)**	1.451	2.556	0.045	0.428
$Zn_{Li2}\_V_{Li1}$**(x)**	1.460	4.646	0.035	0.750
$Zn_{Li2}\_V_{Li0}$**(xxiv)**	1.460	7.180	0.019	0.504
$Zn_{Li2}\_V_{Li1}$**(viii)**	1.460	4.646	0.035	0.750
$Zn_{Li2}\_V_{Li1}$**(vii)**	1.460	4.646	0.035	0.750
$Zn_{Li2}\_V_{Li1}$**(ix)**	1.460	4.646	0.035	0.750
$Zn_{Li2}\_V_{Li1}$**(vi)**	1.461	7.993	0.046	0.730
$Zn_{Li2}\_V_{Li1}$**(xii)**	1.461	4.854	0.046	0.730
$Zn_{Li2}\_V_{Li1}$**(xi)**	1.461	4.854	0.046	0.731
$Zn_{Li2}\_V_{Li1}$**(v)**	1.461	4.854	0.046	0.731
$Zn_{Li2}\_V_{Li0}$**(xxvi)**	1.464	2.556	0.142	0.878
$Zn_{Li2}\_V_{Li0}$**(xvii)**	1.464	2.556	0.142	0.879
$Zn_{Li2}\_V_{Li0}$**(xxiii)**	1.464	2.556	0.142	0.878
$Zn_{Li2}\_V_{Li0}$**(xiii)**	1.481	8.303	0.022	0.978
$Zn_{Li2}\_V_{Li0}$**(xxvii)**	1.481	6.126	0.022	0.975
$Zn_{Li2}\_V_{Li0}$**(xxii)**	1.481	6.126	0.022	0.978
$Zn_{Li2}\_V_{Li0}$**(xx)**	1.481	6.382	0.022	0.978
$Zn_{Li2}\_V_{Li0}$**(xxv)**	1.482	7.617	0.016	0.975
$Zn_{Li2}\_V_{Li0}$**(xv)**	1.482	7.180	0.016	0.975
$Zn_{Li2}\_V_{Li0}$**(xviii)**	1.482	5.976	0.016	0.975
$Zn_{Li2}\_V_{Li0}$**(xvix)**	1.493	5.135	0.025	0.847
$Zn_{Li2}\_V_{Li0}$**(xxi)**	1.493	5.135	0.025	0.847
$Zn_{Li2}\_V_{Li0}$**(xiv)**	1.493	7.203	0.025	0.847
$Zn_{Li2}\_V_{Li0}$**(xxviii)**	1.493	8.950	0.025	0.847
$Zn_{Li2}\_V_{Li2}$**(iv)**	1.597	6.351	0.000	1.114
$Zn_{Li2}\_V_{Li2}$**(i)**	1.597	7.340	0.046	1.112
$Zn_{Li2}\_V_{Li2}$**(ii)**	1.608	7.340	0.000	1.252

Table A3: *Dopant Li-Site Comparison*

Structure	E_0	E_{diff}	E_f	E_f/**f.u.**
LLZO	-715.806	0.0000	N/A	N/A
$Al_{Li2}\_V_{Li0}\_V_{Li0}$	-712.879	2.927	5.395	1.349
$Al_{Li2}\_V_{Li0}\_V_{Li1}$	-712.620	3.185	5.654	1.413
$Al_{Li2}\_V_{Li0}\_V_{Li2}$	-712.135	3.670	6.139	1.535
$Al_{Li2}\_V_{Li1}\_V_{Li1}$	-712.594	3.212	5.680	1.420
$Al_{Li2}\_V_{Li1}\_V_{Li2}$	-712.102	3.704	6.172	1.543
$Al_{Li2}\_V_{Li2}\_V_{Li2}$	-711.488	4.318	6.786	1.697
$Al_{Li1}\_V_{Li0}\_V_{Li0}$	-710.937	4.869	7.337	1.834
$Al_{Li1}\_V_{Li0}\_V_{Li1}$	-711.050	4.755	7.224	1.806
$Al_{Li1}\_V_{Li0}\_V_{Li2}$	-710.415	5.391	7.859	1.965
$Al_{Li1}\_V_{Li1}\_V_{Li1}$	-711.282	4.523	6.992	1.748
$Al_{Li1}\_V_{Li1}\_V_{Li2}$	-710.543	5.262	7.731	1.933
$Al_{Li1}\_V_{Li2}\_V_{Li2}$	-709.943	5.862	8.331	2.083
$Al_{Li0}\_V_{Li0}\_V_{Li0}$	-711.515	4.291	6.759	1.690
$Al_{Li0}\_V_{Li0}\_V_{Li1}$	-711.429	4.376	6.845	1.711
$Al_{Li0}\_V_{Li0}\_V_{Li2}$	-710.867	4.939	7.407	1.852
$Al_{Li0}\_V_{Li1}\_V_{Li1}$	-711.566	4.240	6.708	1.677
$Al_{Li0}\_V_{Li1}\_V_{Li2}$	-710.938	4.868	7.336	1.834
$Al_{Li0}\_V_{Li2}\_V_{Li2}$	-710.240	5.565	8.034	2.008
$Mg_{Li2}\_V_{Li0}$	-712.697	3.109	5.356	1.339
$Mg_{Li2}\_V_{Li1}$	-712.593	3.212	5.459	1.365
$Mg_{Li2}\_V_{Li2}$	-712.105	3.700	5.948	1.487
$Mg_{Li1}\_V_{Li0}$	-712.268	3.537	5.784	1.446
$Mg_{Li1}\_V_{Li1}$	-712.367	3.439	5.686	1.421
$Mg_{Li1}\_V_{Li2}$	-711.784	4.022	6.269	1.567
$Mg_{Li0}\_V_{Li0}$	-712.310	3.495	5.742	1.436
$Mg_{Li0}\_V_{Li1}$	-712.412	3.393	5.640	1.410
$Mg_{Li0}\_V_{Li2}$	-711.821	3.984	6.231	1.558
$Zn_{Li2}\_V_{Li0}$	-710.329	5.476	5.804	1.451
$Zn_{Li2}\_V_{Li1}$	-709.180	6.626	6.953	1.738
$Zn_{Li2}\_V_{Li2}$	-710.291	5.515	5.843	1.461
$Zn_{Li1}\_V_{Li0}$	-709.746	6.060	6.387	1.597
$Zn_{Li1}\_V_{Li1}$	-709.655	6.150	6.478	1.619
$Zn_{Li1}\_V_{Li2}$	-709.098	6.708	7.035	1.759
$Zn_{Li0}\_V_{Li0}$	-709.758	6.048	6.375	1.594
$Zn_{Li0}\_V_{Li1}$	-709.850	5.955	6.283	1.571
$Zn_{Li0}\_V_{Li2}$	-709.286	6.520	6.848	1.712

Table A4: *Dopant La-site Comparison*

Structure	E_0	E_{diff}	E_f	E_f/**f.u.**
Al_{La4}	-709.531	6.275	8.510	2.127
Mg_{La4}+Li_i(**0**)	-711.226	4.580	6.593	1.648
Mg_{La4}+Li_i(**xiv**)	-709.180	6.626	8.640	2.160
Zn_{La4}+Li_i(**0**)	-708.922	6.884	6.978	1.745
Zn_{La4}+Li_i(**xiv**)	-706.148	9.658	9.752	2.438
Al3	-710.920	4.886	7.121	1.780
Mg_{La3}+Li_i(**0**)	-711.482	4.323	6.337	1.584
Mg_{La3}+Li_i(**xiv**)	-710.314	5.491	7.505	1.876
Zn_{La3}+Li_i(**0**)	-709.118	6.688	6.782	1.695
Zn_{La3}+Li_i(**xiv**)	-707.632	8.174	8.268	2.067

Table A5: *Dopant Zr-site Comparison*

Structure	E_0	E_{diff}	E_f	E_f/**f.u.**
Al_{Zr5}+Li_i(**0**)	-710.085	5.720	8.686	2.172
Al_{Zr5}+Li_i(**x**)	-711.088	4.717	7.683	1.921
Al_{Zr5}+Li_i(**xiii**)	-710.052	5.754	8.720	2.180
Al_{Zr5}+Li_i(**xv**)	-710.754	5.052	8.018	2.004
Al_{Zr5}+Li_i(**ii**)	-710.378	5.428	8.394	2.098
Mg_{Zr5}+Li_i(**x**)+Li_i(**xiii**)	-709.596	6.210	8.955	2.239
Mg_{Zr5}+Li_i(**x**)+Li_i(**xv**)	-710.082	5.723	8.468	2.117
Mg_{Zr5}+Li_i(**ii**)+Li_i(**xv**)	-709.666	6.140	8.884	2.221
Zn_{Zr5}+Li_i(**x**)+Li_i(**xv**)	-707.063	8.742	9.567	2.392
Zn_{Zr5}+Li_i(**x**)+Li_i(**xv**)	-707.149	8.657	9.482	2.370
Zn_{Zr5}+Li_i(**ii**)+Li_i(**xv**)	-705.848	9.958	10.783	2.696

Table A6: *Interstitial Energy to Distance and Displacement*

Structure	E_f/**f.u.**	**Distance (Å)**	d_{sum}	d_{vector} **(Å)**
Zn_{La4}+Li_i**(0)**	1.745	2.302	1.260	1.760
Zn_{La4}+Li_i**(i)**	1.756	2.559	1.213	1.979
Zn_{La4}+Li_i**(xiii)**	2.022	2.741	0.930	1.954
Zn_{La4}+Li_i**(x)**	2.030	4.237	0.411	1.749
Zn_{La4}+Li_i**(xii)**	2.064	3.719	0.414	1.946
Zn_{La4}+Li_i**(iii)**	2.083	5.083	0.913	1.704
Zn_{La4}+Li_i**(ii)**	2.122	4.151	0.820	1.780
Zn_{La4}+Li_i**(xv)**	2.213	5.320	0.320	2.035
Zn_{La4}+Li_i**(iv)**	2.305	6.145	0.369	1.994
Zn_{La4}+Li_i**(v)**	2.337	6.830	0.404	1.822
Zn_{La4}+Li_i**(vi)**	2.349	4.824	0.456	1.936
Zn_{La4}+Li_i**(viii)**	2.381	6.261	0.573	1.659
Zn_{La4}+Li_i**(vii)**	2.394	6.167	0.307	1.514
Zn_{La4}+Li_i**(ix)**	2.398	6.379	0.103	1.585
Zn_{La4}+Li_i**(xi)**	2.420	3.874	0.325	2.098
Zn_{La4}+Li_i**(xiv)**	2.438	5.723	0.280	1.922

B.2 Displacement

Table A7: *Zn-doping at the Li2 with the displacement factor for all vacancy sites. Here, f_{atom} is the factor on a scale of 0 to 1 of total displacement force magnitude contributed by atom type.*

Structure	E_f	f_{Li}	f_{La}	f_{Zr}	f_O	f_{Zn}
$Zn_{Li2}\_V_{Li0}$**(xvi)**	1.451	0.298	0.237	0.142	0.280	0.043
$Zn_{Li2}\_V_{Li1}$**(x)**	1.460	0.302	0.266	0.119	0.305	0.009
$Zn_{Li2}\_V_{Li0}$**(xxiv)**	1.460	0.385	0.177	0.092	0.339	0.008
$Zn_{Li2}\_V_{Li1}$**(viii)**	1.460	0.302	0.266	0.119	0.305	0.009
$Zn_{Li2}\_V_{Li1}$**(vii)**	1.460	0.302	0.266	0.119	0.305	0.009
$Zn_{Li2}\_V_{Li1}$**(ix)**	1.460	0.302	0.266	0.119	0.305	0.009
$Zn_{Li2}\_V_{Li1}$**(vi)**	1.461	0.285	0.256	0.162	0.285	0.011
$Zn_{Li2}\_V_{Li1}$**(xii)**	1.461	0.285	0.256	0.162	0.285	0.011
$Zn_{Li2}\_V_{Li1}$**(xi)**	1.461	0.285	0.256	0.162	0.285	0.011
$Zn_{Li2}\_V_{Li1}$**(v)**	1.461	0.285	0.256	0.162	0.285	0.011
$Zn_{Li2}\_V_{Li0}$**(xxvi)**	1.464	0.314	0.232	0.127	0.295	0.032
$Zn_{Li2}\_V_{Li0}$**(xvii)**	1.464	0.314	0.232	0.127	0.295	0.032
$Zn_{Li2}\_V_{Li0}$**(xxiii)**	1.464	0.314	0.232	0.127	0.295	0.032
$Zn_{Li2}\_V_{Li0}$**(xiii)**	1.481	0.321	0.217	0.163	0.295	0.005
$Zn_{Li2}\_V_{Li0}$**(xxvii)**	1.481	0.320	0.217	0.163	0.295	0.005
$Zn_{Li2}\_V_{Li0}$**(xxii)**	1.481	0.321	0.217	0.163	0.295	0.005
$Zn_{Li2}\_V_{Li0}$**(xx)**	1.481	0.321	0.217	0.163	0.295	0.005
$Zn_{Li2}\_V_{Li0}$**(xxv)**	1.482	0.330	0.240	0.139	0.288	0.003
$Zn_{Li2}\_V_{Li0}$**(xv)**	1.482	0.330	0.240	0.139	0.288	0.003
$Zn_{Li2}\_V_{Li0}$**(xviii)**	1.482	0.330	0.240	0.139	0.288	0.003
$Zn_{Li2}\_V_{Li0}$**(xvix)**	1.493	0.328	0.261	0.140	0.266	0.006
$Zn_{Li2}\_V_{Li0}$**(xxi)**	1.493	0.328	0.261	0.140	0.266	0.006
$Zn_{Li2}\_V_{Li0}$**(xiv)**	1.493	0.328	0.261	0.140	0.266	0.006
$Zn_{Li2}\_V_{Li0}$**(xxviii)**	1.493	0.328	0.261	0.140	0.266	0.006
$Zn_{Li2}\_V_{Li2}$**(iv)**	1.597	0.440	0.193	0.119	0.248	0.000
$Zn_{Li2}\_V_{Li2}$**(i)**	1.597	0.417	0.199	0.142	0.242	0.000
$Zn_{Li2}\_V_{Li2}$**(ii)**	1.608	0.509	0.130	0.107	0.253	0.000

Table A8: *Zn-doping at the La4 site with the displacement factor for all interstitial sites. Here, f_{atom} is the factor on a scale of 0 to 1 of total displacement force magnitude contributed by atom type.*

Structure	E_f	f_{Li}	f_{La}	f_{Zr}	f_O	f_{Zn}
Zn_{La4}+Li_i**(0)**	1.745	0.295	0.242	0.148	0.303	0.011
Zn_{La4}+Li_i**(i)**	1.756	0.311	0.247	0.149	0.291	0.002
Zn_{La4}+Li_i**(xiii)**	2.022	0.320	0.184	0.154	0.329	0.013
Zn_{La4}+Li_i**(x)**	2.030	0.371	0.162	0.125	0.328	0.015
Zn_{La4}+Li_i**(xii)**	2.064	0.423	0.145	0.125	0.298	0.009
Zn_{La4}+Li_i**(iii)**	2.083	0.303	0.211	0.143	0.338	0.005
Zn_{La4}+Li_i**(ii)**	2.122	0.324	0.207	0.138	0.325	0.006
Zn_{La4}+Li_i**(xv)**	2.213	0.351	0.180	0.136	0.324	0.009
Zn_{La4}+Li_i**(iv)**	2.305	0.312	0.191	0.137	0.353	0.007
Zn_{La4}+Li_i**(v)**	2.337	0.275	0.238	0.169	0.314	0.003
Zn_{La4}+Li_i**(vi)**	2.349	0.275	0.229	0.154	0.335	0.007
Zn_{La4}+Li_i**(viii)**	2.381	0.257	0.229	0.189	0.321	0.004
Zn_{La4}+Li_i**(vii)**	2.394	0.281	0.226	0.184	0.305	0.004
Zn_{La4}+Li_i**(ix)**	2.398	0.305	0.253	0.164	0.277	0.001
Zn_{La4}+Li_i**(xi)**	2.420	0.301	0.248	0.151	0.295	0.006
Zn_{La4}+Li_i**(xiv)**	2.438	0.298	0.234	0.165	0.296	0.008

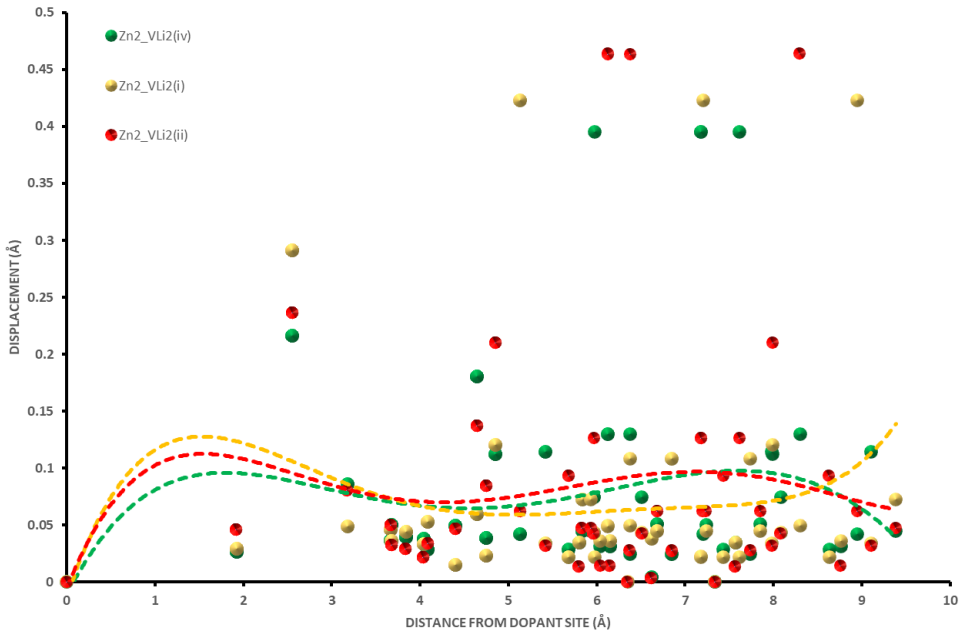

Figure 26: *A comparison of atom distance from the doping site vs displacement of the three Li2 site vacancy structures. The attempt here is to elucidate the minor structural distortions that differentiate the V_{Li2} sites in energy. Non-essential data, but mildly interesting.*

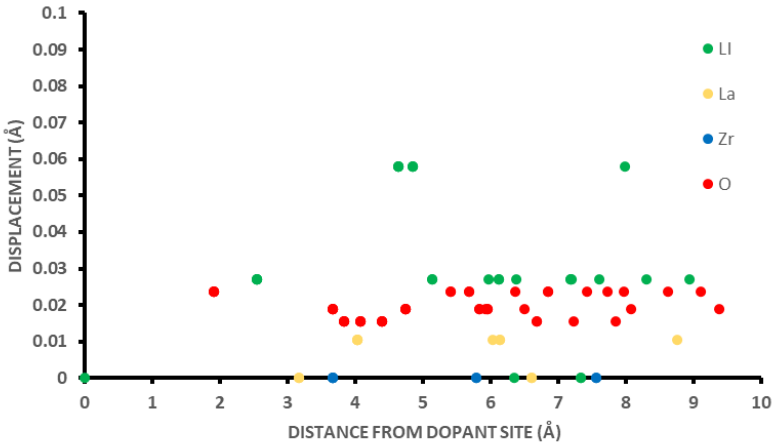

Figure 27: *Stoichiometric LLZO*

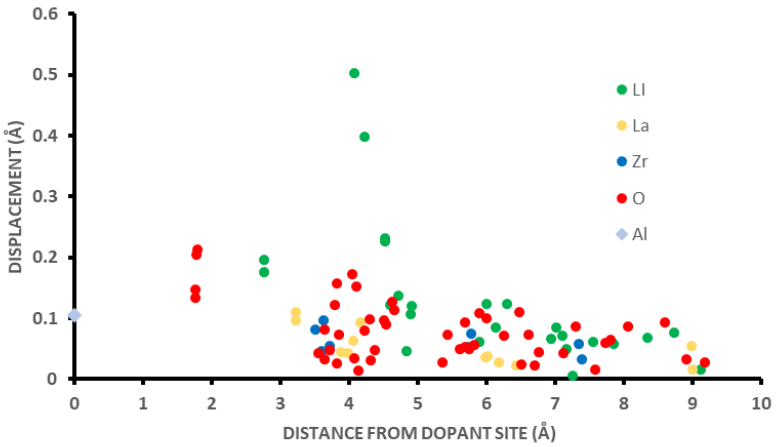

Figure 28: $Al_{Li2}\_V_{Li0}\_V_{Li0}$

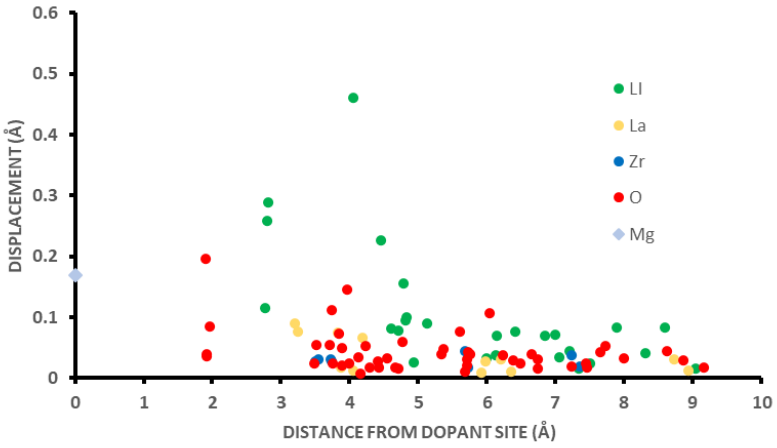

Figure 29: $Mg_{Li2}\_V_{Li0}$

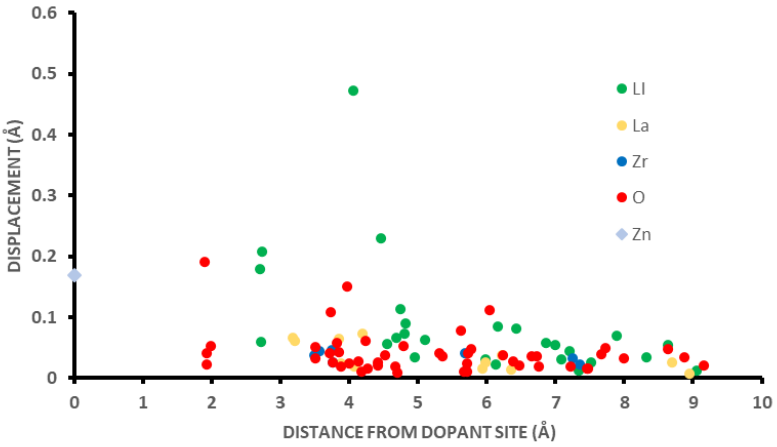

Figure 30: $Zn_{Li2}\_V_{Li0}$

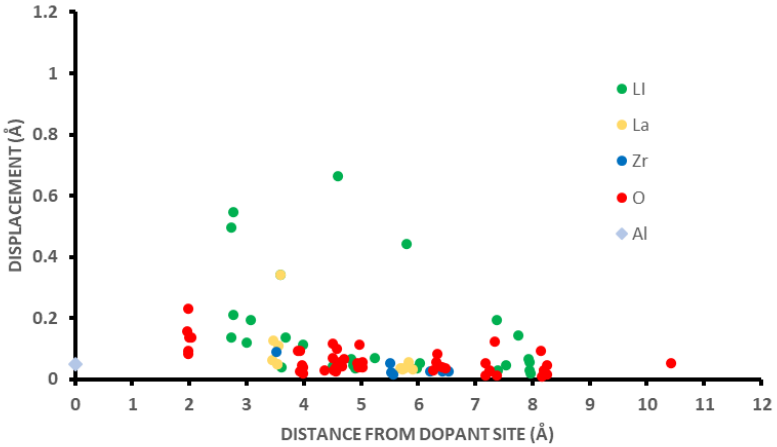

Figure 31: *Al3*

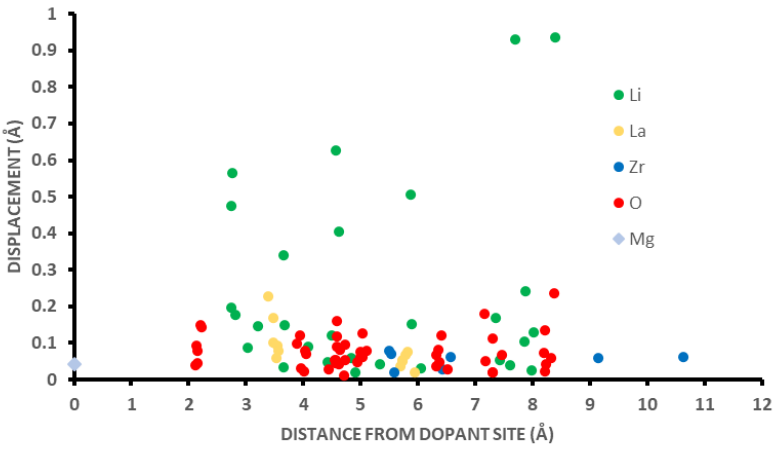

Figure 32: $Mg_{La3}+Li_{0i}$

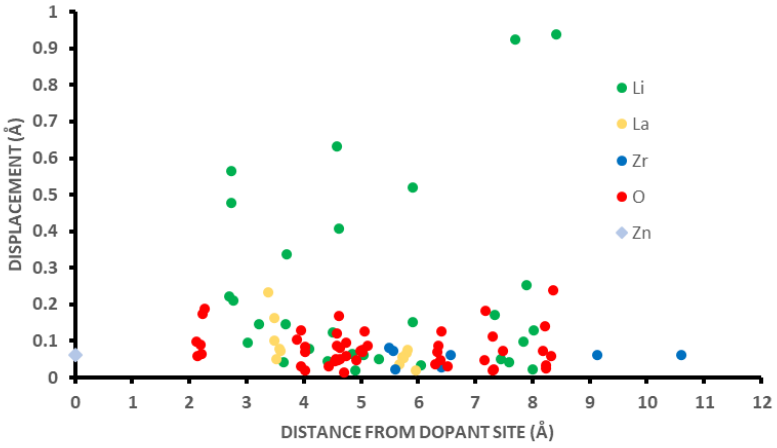

Figure 33: $Zn_{La3}+Li_{0i}$

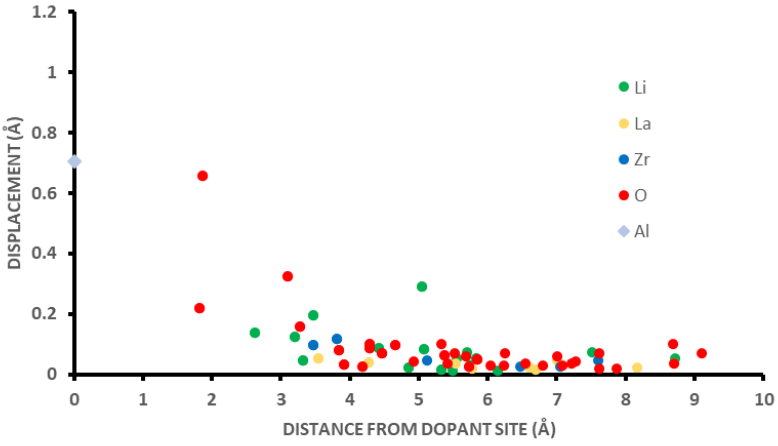

Figure 34: $Al_{Zr5}+Li_{10i}$

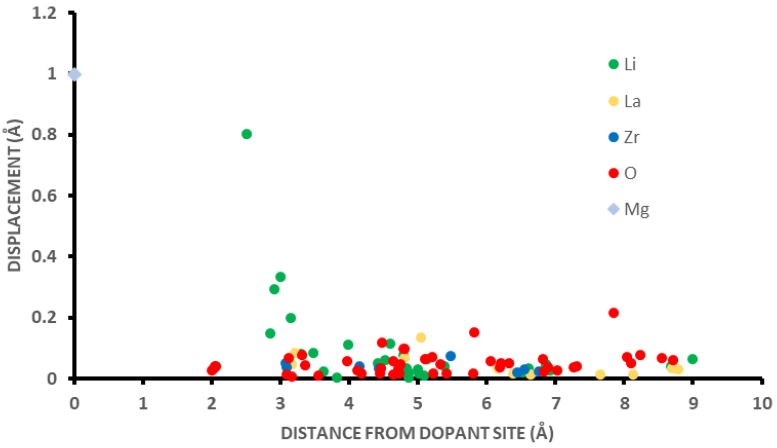

Figure 35: $Mg_{Zr5}+Li_{10i}+Li_{15i}$

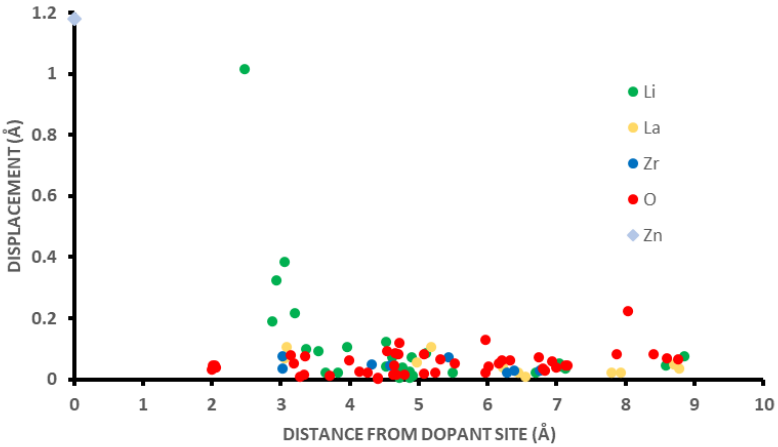

Figure 36: $Zn_{Zr5}+Li_{10i}+Li_{15i}$

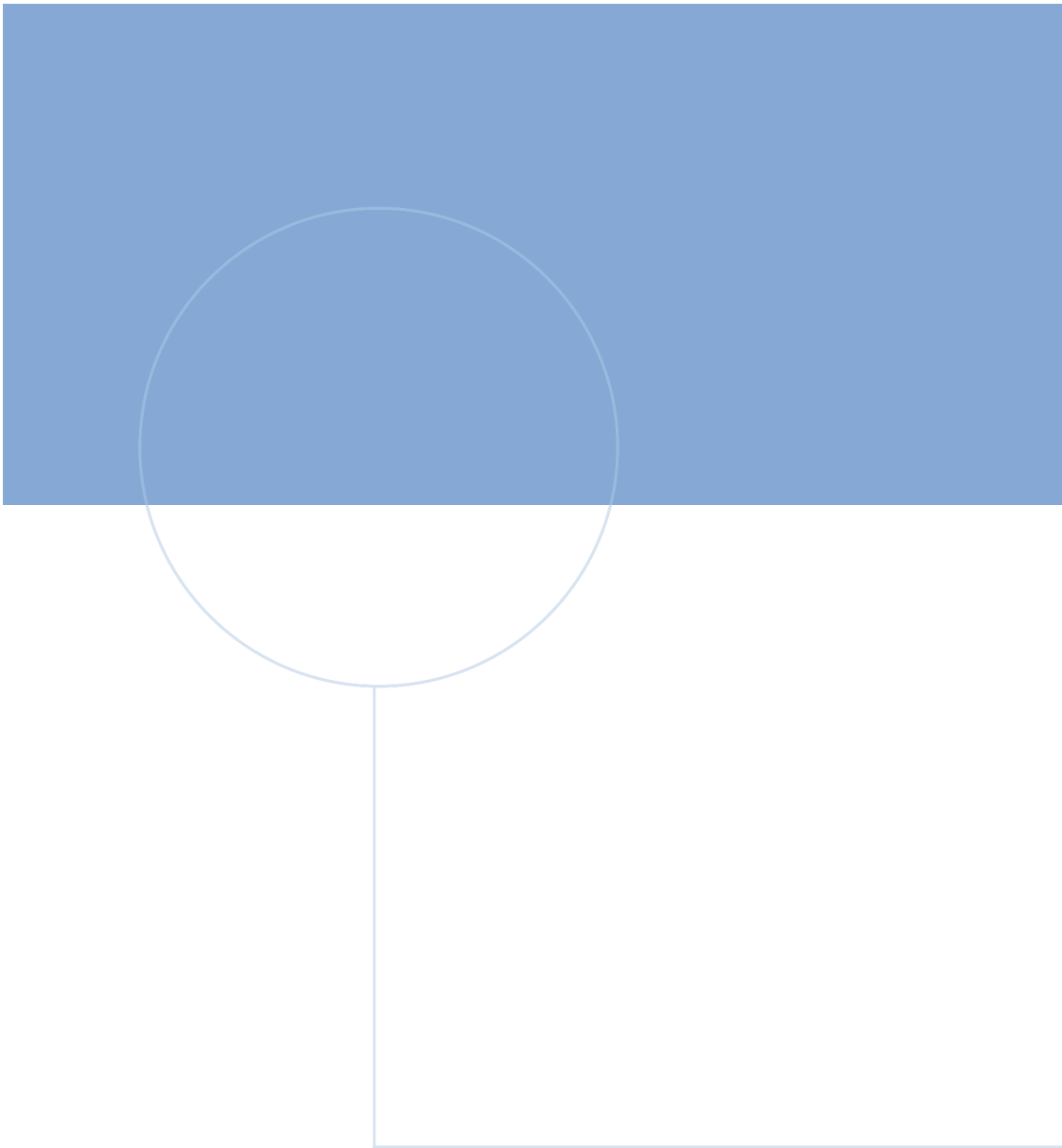

NTNU

Norwegian University of
Science and Technology